Charge transport mechanisms in inkjet-printed thin-film transistors of two-dimensional materials

Erik Piatti,[1,*] Adrees Arbab,[2,3,*] Francesco Galanti,[1] Tian Carey,[3] Luca Anzi,[4] Dahnan Spurling,[5] Ahin Roy,[5] Ainur Zhussupbekova,[5] Kishan A. Patel,[4] Jong M. Kim,[6] Dario Daghero,[1] Roman Sordan,[4] Valeria Nicolosi,[5] Renato S. Gonnelli,[1] and Felice Torrisi[3,†]

[1] *Department of Applied Science and Technology, Politecnico di Torino, I-10129 Torino, Italy*
[2] *Cambridge Graphene Centre, University of Cambridge, Cambridge CB3 0FA, UK*
[3] *Department of Chemistry, Molecular Sciences Research Hub, Imperial College London, White City Campus, Wood Lane, London, W12 0BZ, UK*
[4] *L-NESS, Department of Physics, Politecnico di Milano, I-22100 Como, Italy*
[5] *Trinity College Dublin, Dublin 2, Ireland*
[6] *Department of Engineering, University of Cambridge, Cambridge CB3 0FA, UK*

Printed electronics has emerged as a pathway for large scale, flexible, and wearable devices enabled by graphene and two-dimensional (2D) materials. Solution processing of graphite and layered materials demonstrated mass production of inks allowing techniques such as inkjet printing to be used for device fabrication. However, the complexity of the ink formulations and the polycrystalline nature of the thin films, together with the metal, semimetal, and semiconducting behaviour of different 2D materials, have impeded the investigation of charge transport in inkjet printed 2D material devices. Here we unveil the charge transport mechanisms of surfactant- and solvent-free inkjet-printed thin-film devices of representative few-layer graphene (semi-metal), molybdenum disulfide (MoS_2, semiconductor) and titanium carbide MXene (Ti_3C_2, metal) by investigating the temperature (T), gate and magnetic field dependencies of their electrical conductivity. We find that charge transport in printed few-layer MXene and MoS_2 devices is dominated by the intrinsic transport mechanism of the constituent flakes: MXene devices exhibit a weakly-localized 2D metallic behavior at any T, whereas MoS_2 devices behave as insulators with a crossover from 3D-Mott variable-range hopping at low T to nearest-neighbor hopping around at ~ 200 K. The charge transport in printed few-layer graphene devices is dominated by the transport mechanism between different flakes, which exhibit 3D-Mott variable range hopping conduction at any T. These findings reveal and finally establish the fundamental mechanisms responsible for charge transport in inkjet-printed devices with 2D materials, paving the way for a reliable design of high performance printed electronics.

I. INTRODUCTION

Printable inks based on graphene and 2D materials have untapped potential in high performance printed [1–5], flexible [6, 7] and wearable electronics [1, 8, 9]. Electronic inks from 2D materials (E2D inks) are mixtures of a functional 2D material, stabilizers, and rheology modifiers. E2D inks with different electronic properties have been developed to print the different elements of a device: semiconducting or semimetallic inks in the active layer, insulating inks for dielectrics, and conducting inks for electrodes.

Solution-processing techniques such as electrochemical exfoliation [10–12] and liquid-phase exfoliation (LPE), including shear mixing [13], microfluidization [3, 6] and ultrasonication [14–16] have enabled large-scale production of graphene and other E2D inks [2, 3] with the required different electronic properties. Many electronic [1, 17, 18], optoelectronic [19, 20], and photonic [21–23] devices have been demonstrated via several printing methods such as inkjet printing [3, 4, 24], screen printing [6, 25], flexographic printing [26], gravure printing [7], and spray coating [27, 28]. Above all, drop-on-demand (DoD) inkjet printing unleashed the full potential of E2D inks, combining advantages such as versatility to print on wide range of substrates (e.g. textile, polymers and silicon), maskless and non-contact deposition at a high resolution ($\sim 50\ \mu$m) and low material losses (< 1 ml) [29].

Inkjet-printed field-effect transistors (FETs) with E2D inks have demonstrated mobilities of up to $\sim 204\ cm^2V^{-1}s^{-1}$ with graphene inks on Polyethylene terephthalate (PET) substrates [3], while current modulation in printed E2D ink thin films was also achieved using ionic gating with a liquid electrolyte using a spray-coated h-BN layer as a porous separator [4]. Inkjet-printed E2D ink photodetectors [5, 30] achieved photoresponsivities of up to ~ 50 mA W^{-1}, with MoS_2 on Polyimide (PI) [31]. As a result, there is now a substantial industrial interest in using E2D inks for applications in printed wearable electronics and electronic-textiles (e-textiles) [1], currently incompatible with organic or inorganic semiconductors. A technology roadmap for electronics based on E2D inks urges a thorough understanding of the charge transport mechanisms in printed thin films of E2Ds, enabling an accurate description of the device physics [32, 33].

Since the first experiments on graphene [34] the charge transport mechanisms in isolated flakes of 2D materials

* These authors contributed equally.
† Corresponding author: f.torrisi@imperial.ac.uk

have been extensively investigated, ranging all the way from semiconductors such as MoS_2 [35–42], to semimetals such as graphene [43–49], to metals such as MXenes [50–57]. However, the structure of inkjet-printed films consist of a large number of highly-crystalline flakes assembled together in a three-dimensional network [1], and is more complex than that of isolated flakes. As a consequence, the transport in inkjet-printed 2D material films depends on an interplay between charge-carrier propagation within each flake (*intra*-flake transport) and propagation from one flake to the surrounding flakes in the network (*inter*-flake transport) [58]. This makes inkjet-printed films of E2D inks a prime example of granular conductors with 2D material units, and inevitably introduces an additional disorder with respect to that found in isolated flakes in the form of the sharp boundaries between the different printed flakes in the network [2, 59].

The charge transport in a disordered system can in general be divided in two distinct regimes, insulating and metallic. The insulator-to-metal transition (IMT) [60, 61] occurs when the Fermi energy E_F is tuned across the so-called mobility edge [35, 36, 60–63]. In the insulating regime, charge carriers are localized within a length ξ_{loc} [60, 61] and, at finite temperature, can hop between localized states. The average hopping distance R_{hop} is set by the balance between the shortest possible hopping distance and the smallest energy difference of the available localized states [35, 60, 61]. On increasing the temperature, this variable-range hopping (VRH) mechanism crossovers into a nearest-neighbor hopping (NNH) one, in which carriers can hop directly between the closest localized states irrespectively of their energy difference [60, 61]. The conductivity in the metallic regime, on the other hand, is finite even at zero temperature [60, 61] and decreases on increasing temperature [64]. In low-dimensional disordered metals, the low-temperature conductivity [65, 66] can be governed by weak localization (WL) [67, 68], electron-electron interactions (EEI) [69, 70], Kondo effect [71, 72], or a combination thereof. This description, although originally developed for disordered crystalline materials, was subsequently shown to be valid also for granular conductors [73–75] such as granular metals [76, 77], cermets [77–80], metal-cluster and carbon-based composites [81], and recently 2D material networks [82–86].

In this context, gate-, temperature-, and magnetic-field-dependent conductivity measurements are powerful tools to investigate the charge transport properties of disordered materials, by tuning a material across the IMT [36–41, 48, 63, 87–89], discriminating between the different hopping processes in the insulating regime [35, 36, 41, 42, 60–62, 90–95], and defining the interplay of WL, EEI and Kondo effect in the metallic regime [49, 53, 65, 66, 96–107]. An early attempt to probe low-T conductivity of printed thin films of semiconducting transition metal dichalcogenides suggested that charge transport occurred via some kind of hopping mechanism, but failed to reach a conclusion on the specific model [4]. Despite its fundamental importance, the charge transport mechanism in inkjet-printed 2D material devices is thus still unexplored. In this work, we determine the transport mechanisms in metallic, semimetallic and semiconducting inkjet-printed E2D-ink films by performing a comprehensive investigation of the temperature-, gate- and magnetic field-dependent conductivity measurements in inkjet-printed field-effect devices from surfactant-free Ti_3C_2 MXene, graphene and MoS_2 inks composed of few-layer E2D flakes. We demonstrate that in the printed MXene and MoS_2 devices, the charge transport is dominated by *intra*-flake processes and mirrors that in the isolated constituent flakes. Conversely, we show that in the inkjet-printed graphene devices the transport is dominated by *inter*-flake processes and deviates from the semimetallic behavior of isolated graphene.

II. INK FORMULATION AND MATERIAL CHARACTERISATION

Typically E2D ink formulations require the use of additives such as binders (substances which cohesively hold materials together) or surfactants, which degrade the electrical properties of the ink [2, 3, 32] as most of the binders and surfactants hinder the hopping of charge carriers through a film of 2D materials. Solvent-exchange techniques have been successfully adopted on exfoliated layered material dispersions to produce stabiliser-free low boiling point ($< 100°C$) E2D inks in ethanol, for inkjet-printed electronics [3]. Here we adopt the solvent-exchange technique (see Methods) yielding pure graphene, MoS_2 and Ti_3C_2 low-boiling-point inks in ethanol suitable for inkjet-printing. The graphene ink was prepared by ultrasonic exfoliation of graphite (see Methods) following our previous work. [3] The MXene ink was produced by etching the aluminium in MAX powder using the in-situ hydrofluoric acid method (see Methods) [18], while the MoS_2 ink was prepared by electrochemical exfoliation of bulk MoS_2 layered crystals via quaternary ammonium molecules (see Methods) [11]. We measure the optical absorption spectra in the ultraviolet-visible (UV-Vis) range (Cary 7000 UV-Vis-NIR Spectrometer) to estimate the flake concentration, c, via the Beer-Lambert law (see Methods) for the MXene (Fig. 1a), graphene (Fig. 1b) and MoS_2 (Fig. 1c) inks by using the absorption coefficients $\alpha_{660} \sim 538$ L g^{-1} m^{-1} (as determined in Fig. S1), ~ 2460 L g^{-1} m^{-1} [14], and $\alpha_{672} \sim 3400$ L g^{-1} m^{-1}, respectively. We obtain $c_{MX} \sim 0.50$ mg ml^{-1}, $c_{GR} \sim 0.495$ mg ml^{-1} and $c_{MS} \sim 2.73$ mg ml^{-1} for the MXene, graphene and MoS_2 inks, respectively. The UV-Vis spectrum of the graphene ink is mostly featureless as expected [108], with a prominent peak at ~ 268 nm which can be attributed to a signature of the Van Hove singularity in the graphene density of states (DOS) [108]. The UV-Vis spectrum of the MoS_2 ink shows the characteristic A (~ 610 nm) and

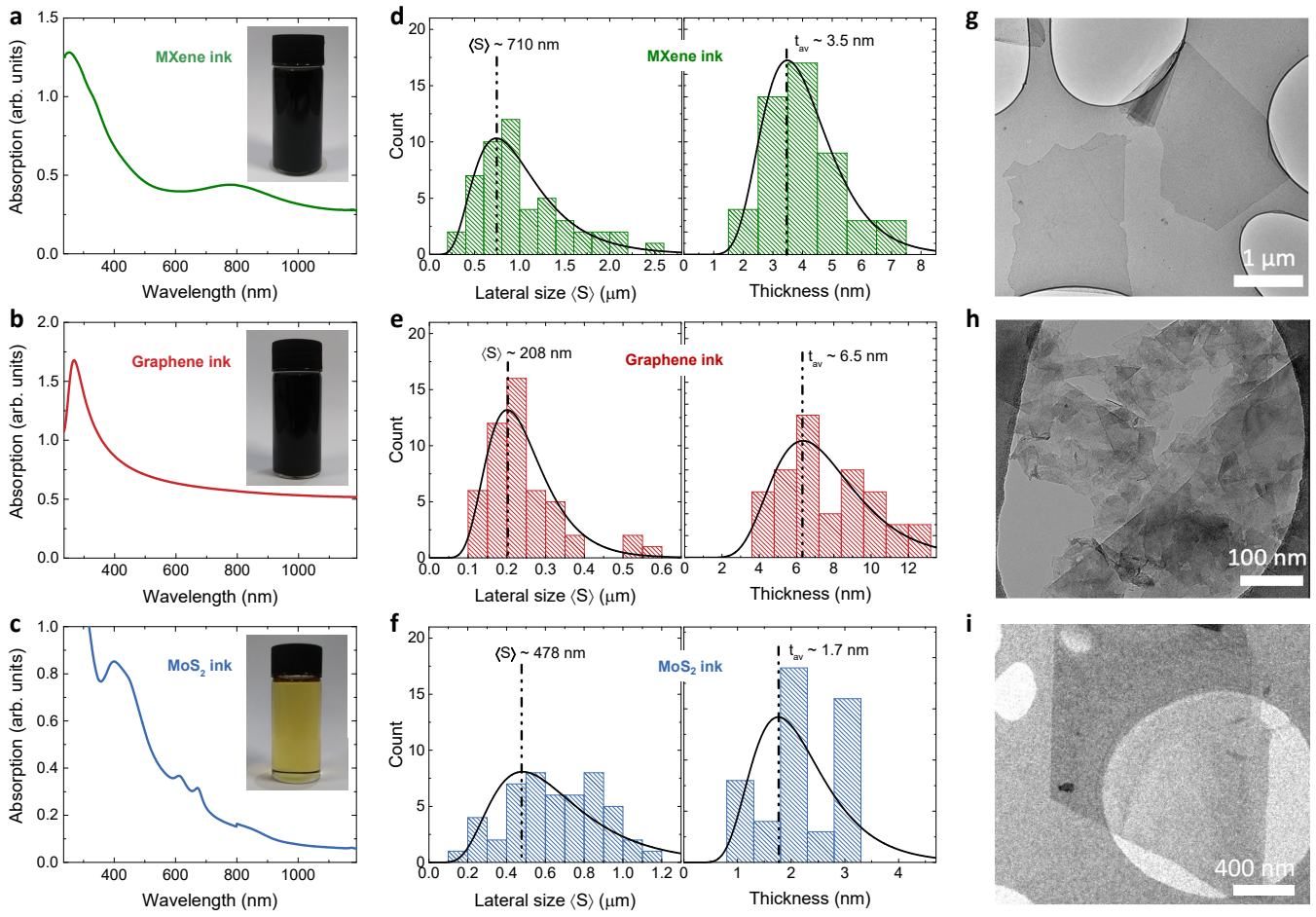

FIG. 1. Ultraviolet spectroscopy of **a** the MXene, **b** the graphene, and **c** the MoS_2 inks used to make thin films. Insets show the photographs of the corresponding solvent-dispersed 2D material flakes. Statistics of the lateral size and thickness of **d** the MXene, **e** the graphene, and **f** the MoS_2 flakes in the E2D inks. Transmission electron microscope image of **g** the MXene, **h** the graphene, and **i** the MoS_2 flakes in the E2D inks.

B ($\sim$ 675 nm) excitonic peaks of the 2*H* semiconducting crystal phase [109], as well as a broader feature at $\sim$ 420 nm due to the convolution of the C and D excitonic peaks [110]. The UV-Vis spectrum of the MXene ink shows a distinct peak at $\sim$ 260 nm which originates from surface termination groups (-F, -OH and -O) [111, 112], originating during the etching process (see Methods) [113]. The MXene ink also has a broad peak at $\sim$ 800 nm which is associated to a transversal surface plasmon in the MXene flakes [56, 114, 115], which is greatly enhanced upon functionalisation of their surface with aluminium (Al) oxoanion groups [116]. We employ energy-dispersive X-ray spectroscopy (EDX) to confirm the removal of Al from the MAX phase precursor during the etching process to form the MXene ink (see Fig. S2). The EDX shows that the Al signal at $\sim$ 1 keV is substantially weak compared to that of titanium (Ti) and carbon (C), and comparable to the signal obtained for high-quality Ti_3C_2 MXenes in previous reports [111–113]. We then validate the suitability of the inks for inkjet printing using these parameters to calculate the figure of merit Z (see Methods) [117], finding $Z_{GR} \sim 22$, $Z_{MS} \sim 11$ and $Z_{MX} \sim 4$ for for graphene, MoS_2 and MXene inks respectively, in accordance with previous reports on inkjet-printed E2D inks [3, 24].

The lateral size $\langle S \rangle = \sqrt{xy}$, where x and y represents length and width of the flakes, and average thickness t_{av} of the 2D-material flakes are estimated by atomic force microscopy (AFM, Bruker Dimension icon, peak-force mode) by analysing 50 individual flakes (see examples in Figs. S3, S4 and S5) from diluted (by a factor of 100) and drop-cast inks (see Methods). Figs. 1d-f show the statistical distributions of $\langle S \rangle$ and t_{av} in the form of a histogram for MXene, graphene and MoS_2 inks. A log-normal distribution peaked at $\langle S \rangle_{MX} \simeq 710$ nm, $\langle S \rangle_{GR} \simeq 208$ nm and $\langle S \rangle_{MS} \simeq 478$ nm appears for the MXene, graphene and MoS_2 flakes, respectively. This confirms that the flake dimensions fall within the required range for DoD inkjet printing [24]. We also find the average flake thickness for the MXene, graphene and

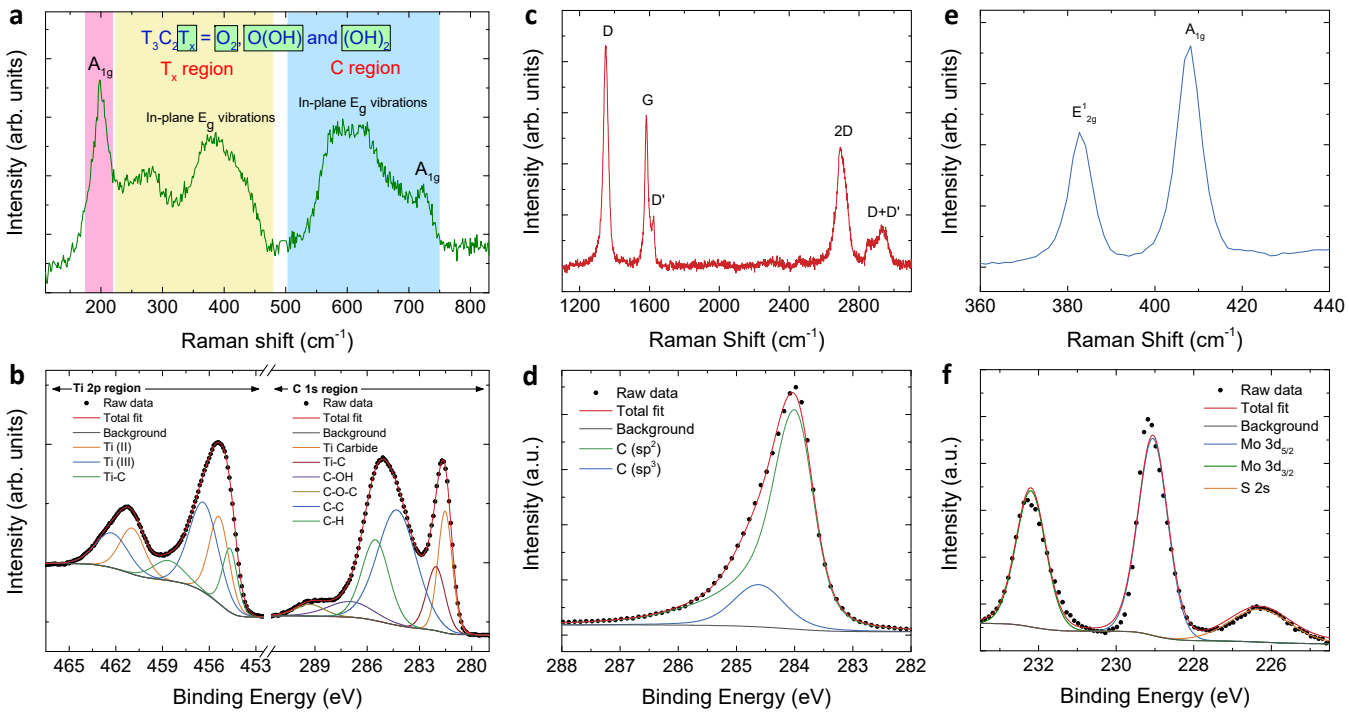

FIG. 2. **a** Raman spectrum of the MXene ink. Blue and pink shaded areas indicate the in-plane and the out-of-plane modes, due either to termination groups (T_x region) or to C atoms (C region). **b** XPS of the MXene ink, showing the C 1s and the Ti 2p regions. **c** Raman spectrum of the graphene ink and **d** its XPS, showing the carbon region comprising sp^2 and sp^3 carbon atoms. **e** Raman spectra of the MoS_2 ink **f** and its XPS showing the molybdenum region. All Raman spectra were acquired at 514.5 nm.

MoS_2 inks to be $t_{av,MX} \simeq 3.5$ nm, $t_{av,GR} \simeq 6.5$ nm and $t_{av,MS} \simeq 1.7$ nm. Transmission electron microscopy (TEM) corroborates the distribution of the lateral size of the flakes in the inks (Figs. 1g-i), showing that the MXene inks can have flakes with $\langle S \rangle \geq 1$ μm, whereas the graphene and MoS_2 flakes tend to be in the range of $\langle S \rangle \simeq 200 - 900$ nm.

We then employ Raman spectroscopy (Renishaw 1000 InVia micro-Raman) to examine the structural quality of the E2D flakes and X-ray photoelectron spectroscopy (XPS, K-Alpha, Thermo Scientific) to assess their stochiometry. Raman spectra are acquired at a wavelength (λ) of 514.5 nm. Both analyses are carried out on inks drop-cast on a Si/SiO_2 substrate (see Methods).

In the MXene ink, the Raman spectrum (Fig. 2a) shows two broad resonant regions, denoted as the T_x region betweeen ~ 223 cm^{-1} and ~ 480 cm^{-1}, and the C region between ~ 503 cm^{-1} and 750 cm^{-1}. The T_x region comprises convoluted peaks corresponding to the modes originating from the different termination groups present on the surface of a MXene flakes, and denoted as T_x. These terminations can be O_2, O(OH) or $(OH)_2$ [118], and the convoluted peaks in the T_x region originate from E_g in-plane modes (light yellow shaded area) [118]. The C region comprises of a collection of convoluted peaks that originate from E_g in-plane modes and A_{1g} out-of-plane modes (blue shaded area) of the carbon atoms in the Ti_3C_2 MXene [118]. An additional peak appears at ~ 205 cm^{-1} and is caused by an A_{1g} out-of-plane vibrational mode that originates from the carbon atoms, the two titanium layers and the functional -OH, O and -F surface groups [119]. This is confirmed by the EDX spectra (see Methods) showing the presence of -O, -F and minor traces of -Cl (see Fig. S2). Fig. 2b shows the XPS spectrum of the C 1s and Ti 2p regions for the MXene ink, that confirm the formation of Ti_3C_2 from the MAX phase powder. The C 1s region comprises six non-doublet peaks; the largest of the peaks at ~ 285 eV belongs to graphitic C-C formation that occurs due to selective dissolution of Ti during etching [120, 121]. The peaks at 281.5 eV and 282.1 eV are indicative of Ti carbide and Ti-C bonds. Whereas, the smaller peaks at 287.2 eV and 289.2 eV are due to the presence of C-OH and C-O-C bonds, in agreement with the Raman and EDX data. The peak at 285.8 eV is associated with the C-H functional group on the surface of the MXene flakes. The Ti 2p region contains three doublet peaks: The Ti (II)($2p_{3/2}$ ~ 455 eV and $2p_{1/2} \sim 461$ eV) and the Ti (III) ($2p_{3/2}$ ~ 457 eV and $2p_{1/2} \sim 462.5$ eV) doublets, arising from the $Ti_3C_2O_x$ and $Ti_3C_2(HO)$ functional groups on the MXene flake surface [119, 122]. The asymmetric Ti-C ($2p_{3/2} \sim 454.8$ eV and $2p_{1/2} \sim 460$ eV) peak which is commonly associated with MXene flakes is shifted to a larger binding energy compared to its precursor MAX

phase powder. This is attributed to the Al in the MAX phase powder (Ti-C $2p_{3/2}$ ∼ 454.6 eV) being replaced by a more electronegative termination group like -F, -O, and -OH [120, 122–124].

The Raman spectrum of the graphene ink (Fig. 2c) shows the characteristic G peak at 1581 cm^{-1} that corresponds to the in-plane E_{2g} phonon [125]. Additionally, the D peak and Lorentzian-shaped 2D peak positioned at ∼ 1349 cm^{-1} and ∼ 2700 cm^{-1} respectively, indicate that the graphene film comprises electronically-decoupled graphene layers. In pristine graphene inks, the D peak corresponds to the edges of the submicrometer flakes, rather than to the presence of a large amount of disorder within the flakes [24, 126]. The D+D′ peak at ∼ 2950 cm^{-1} is also present and it is attributed to a two-photon defect-assisted process [127]. The XPS spectrum of the graphene ink (Fig. 2d) shows a convoluted peak, composed of two peaks associated with the sp^2 and sp^3 carbon atoms [128, 129]. The sp^2 peak (green curve) at ∼ 283.9 eV has a broad and asymmetric tail at higher binding energies, which is not present in the case of the sp^3 peak (blue curve) at ∼ 284.7 eV. The area under the sp^2 and sp^3 peaks can be used to quantify the ratio of sp^2 and sp^3 carbon atoms present in the measured sample. A high sp^2 content would be indicative of a more pristine graphene film [6]. Integrating the area under the curve reveals a ratio of 80% : 20% (sp^2 : sp^3), which implies that the majority of C atoms are sp^2 hybridised.

In the MoS_2 ink, the Raman spectrum (Fig. 2e) shows the typical E^1_{2g} and A_{1g} peaks that appear at ∼ 382.5 and 406.8 cm^{-1}, respectively. The position of both peaks indicates a high crystallinity of the flakes [130]. Fig. 2f shows the XPS spectrum of the MoS_2 inks, which exhibits the $3d^{3/2}$ and $3d^{5/2}$ doublet peaks associated with molybdenum (Mo) that appear at ∼ 232 eV and ∼229 eV, respectively. The XPS spectrum also shows a 2s peak originating from the sulfur (S) atoms in MoS_2 [131].

III. INKJET-PRINTED 2D MATERIAL THIN-FILM DEVICES

We fabricate the graphene and MXene thin-film devices by inkjet printing (Fujifilm Dimatix DMP-2800, see Methods) the graphene and MXene inks on p-doped Si/SiO_2 substrates in the form of rectangular strips (≈ 4 mm × 2 mm). We additionally fabricate flexible graphene films on PET as detailed in Ref. 3 for comparison. The MoS_2 thin-film devices were printed on a pre-patterned substrate as described in the Methods section. The low boiling point of our E2D inks improve the morphological uniformity and assist in the solvent removal after printing [27]. When inkjet printing, the ejected drop contacts the substrate as discussed in the Supplementary Information and Figs. S6 and S7. AFM and profilometer data show that the rectangular printed films of graphene, MXene, and MoS_2 inks have a thickness of $t_{d,GR}$ ∼ 130 nm, $t_{d,MX}$ ∼ 30 nm and $t_{d,MS}$ ∼ 40 nm (see Figs. S3, S4 and S5), which were selected to ensure that the percolation threshold for each E2D ink is achieved [132, 133]. Before measuring the thickness of the films, the graphene and MXene devices were annealed at 250 °C and 80 °C for 45 s, respectively to remove any potential trapped solvent, whereas the MoS_2 film was annealed at 400 °C for 60 min, to remove PVP (see Methods). All the E2D devices were annealed in nitrogen atmosphere to avoid oxidation.

The inkjet-printed thin film devices were then contacted for charge transport measurements (see Methods), as shown schematically in Figs. 3a,b for graphene/MXene and MoS_2 devices, respectively. In the printed MXene and graphene devices, the Ag contacts were directly deposited on the rectangular printed films (see Methods) defining source (S), drain (D) and four-probe voltage (V_{xx}) contacts, while the gate voltage, V_G, was applied directly through the p-doped Si substrate (see Fig. 3a). The printed MoS_2 were electrically connected via the pre-patterned Ti/Au source and drain contacts (see Fig. 3b). A V_G was applied via an Al electrode through a thin AlO_x layer (see Methods), which has previously shown to improve the modulation of inkjet-printed MoS_2 FETs [134] compared to inkjet-printed MoS_2 devices gated through SiO_2/Si stacks [85]. In the selected printed MoS_2 devices, a small droplet of DEME-TFSI ionic liquid was optionally drop-cast on the device channel and a gold side-gate electrode was used to apply V_G as the ionic-gate voltage. The insets to Fig. 3c show the optical images of the three representative printed MXene (green border), graphene (red border), and MoS_2 (blue border) devices.

IV. CHARGE TRANSPORT IN INKJET-PRINTED E2D-INK DEVICES

We investigate the charge transport mechanisms in the inkjet-printed E2D-ink field-effect devices by measuring the conductivity σ as a function of temperature T (see Methods). Fig. 3c plots σ as a function of T for the inkjet printed MXene (green curve), graphene (red curve) and MoS_2 (blue curve) thin film devices at $V_G = 0$. At $T = 290$ K, the conductivity of the inkjet-printed devices spans over five orders of magnitude, ranging from $1.7 \cdot 10^{-3}$ $\Omega^{-1}cm^{-1}$ in the MoS_2-ink device, to 1.1 $\Omega^{-1}cm^{-1}$ in the graphene-ink device, to 208 $\Omega^{-1}cm^{-1}$ in the MXene-ink device. Upon cooling, the difference between the conductivity in the three materials increases. Between T ∼ 290 K and ∼50 K, the conductivity of the MoS_2-ink device σ_{MS} decreases by three orders of magnitude, consistent with the behavior of ungated MoS_2 flakes [35–42], and falls below $3 \cdot 10^{-6}$ $\Omega^{-1}cm^{-1}$ for $T \leq 50$ K. In the same T range, the conductivity of graphene-ink devices σ_{GR} also decreases with decreasing T, albeit only by a factor ∼5 between T ∼ 290 K and 5 K, and it differs from the metallic-like behavior typically observed in an individual graphene flake [43–49]. These dependencies of σ_{MS} and σ_{GR} on T suggest that the

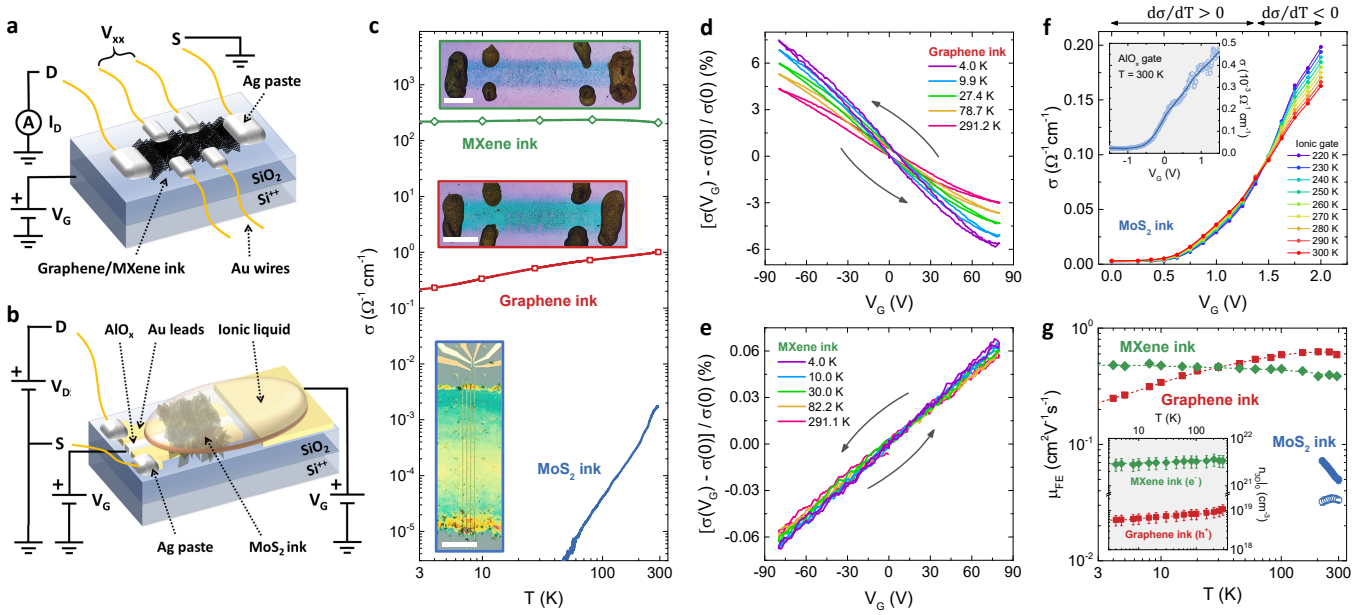

FIG. 3. Sketch of: **a**, an inkjet-printed graphene/MXene field-effect device, and **b**, an inkjet-printed MoS_2 device. **c**, Conductivity σ at $V_G = 0$ as a function of temperature T in E2D-ink FETs, in double logarithmic scale. Solid blue, red and green lines are the σ of a printed MoS_2-ink device, a printed graphene-ink device, and a printed MXene-ink device respectively. Hollow symbols are the values of $\sigma(0)$ for which the V_G sweeps are shown in panels **d**,**e**. Insets show the optical images of a printed MXene device (green border, scale bar 4 mm), a printed graphene device (red border, scale bar 4 mm) and a printed MoS_2 device (blue border, scale bar 100 μm). **d**,**e**, Conductivity ratio $[\sigma(V_G) - \sigma(0)]/\sigma(0)$ as a function of the gate voltage V_G for increasing temperature T in a printed graphene device (**d**) and in a printed MXene device (**e**). Black arrows indicate the direction of the V_G sweeps. **f**, Conductivity σ of a printed MoS_2 device as a function of the gate voltage V_G applied to the ionic gate at different temperatures, constructed by starting from the curves of σ as a function of T at different V_G shown in Fig. 4c. Inset shows σ as a function V_G applied through the AlO_x via the Al gate electrode. **g**, Field-effect mobility μ_{FE} as a function of T in logarithmic scale for a printed graphene device (red squares), a printed MXene device (green diamonds) and a printed MoS_2 device (hollow blue circles, $V_G \lesssim 1.37$ V; filled blue circles, $V_G \gtrsim 1.37$ V). Dashed lines are guides to the eye. The inset shows the intrinsic carrier densities per unit volume $n_{3D}|_0$ as a function of T in graphene and MXene-based devices.

charge transport in both MoS_2-ink and graphene-ink devices occurs via some kind of hopping process [60, 61, 73–75]. In particular, inter-flake hopping is certainly dominant in the case of graphene, since single flakes display a metallic-like behaviour that differs from that observed in our films. In the case of MoS_2, where even the single flakes display an insulating-like behaviour, a deeper analysis is needed to understand whether *inter-* or *intra*-flake hopping mechanisms dominate. Conversely, the conductivity of the MXene-ink device σ_{MX} appears to be nearly T-independent in the scale of Fig. 3c, in line with reports on MXene epitaxial films [53]. The transport in the MXene-ink device should thus occur via conduction over extended states [60, 61, 73–75].

We then consider how the charge transport in our inkjet-printed devices can be tuned in a FET configuration by applying V_G. For printed graphene and MXene devices, we measured the σ response to V_G sweeps between -80 V and +80 V at various temperatures. In Fig. 3d,e we show the gate-dependent conductivity ratio $[\sigma(V_G) - \sigma(0)]/\sigma(0)$ for a limited number of T values for the printed graphene and MXene devices, with the full sets of curves showing σ as a function of V_G being reported in Fig. S8. In both cases, $\sigma(0)$ is the conductivity at $V_G = 0$ shown in Fig. 3c as hollow squares for the printed graphene and MXene devices. The printed graphene devices (Fig. 3d) show σ_{GR} decreasing monotonically with increasing V_G, which indicates that the charge carriers in the graphene flakes are holes, induced by unintentional doping of adsorbed molecules such as water [34, 135]. A finite hysteresis is also observed in the curves, likely stemming from charge transfer with traps close to the graphene-SiO_2 interface [135, 136]. Both intrinsic hole doping and hysteretic behavior in the gate transfer curves have been reported in inkjet-printed graphene transistors [3, 24]. The maximum gate-induced modulation of σ_{GR} increases as T decreases, from 7.5% at 290 K to 13.5% at T~4 K, remaining smaller but in line with earlier reports of source-drain current modulations in inkjet-printed graphene FETs [3, 24, 86]. Fig. 3e shows σ_{MX} increasing monotonically with increasing V_G in the inkjet-printed MXene device, indicating that the charge carriers in the MXene flakes are electrons. Unlike the printed graphene device, we observe no hysteresis in

the transfer curves of the MXene devices. Both findings are in agreement with the FET behavior of single-layer MXene flakes [54, 55]. The maximum gate-induced modulation of σ_{MX} slightly increases as T decreases, from $\sim$0.11% at $T\sim$290 K to $\sim$0.14% at $T\sim$4 K, and is thus about two orders of magnitude smaller than that of the printed graphene devices, consistent with the metallic behavior exhibited by the printed MXene films. The modulation is also small compared to the source-drain current modulations of $\sim$ 1% reported in single-layer MXene FETs [54, 55], and can be ascribed to the much larger thickness of our printed films. For the printed MoS_2 devices, we first measured σ as a function of V_G between -1.5 and $+1.5$ V, applied through the Al/AlO_x gate stack at $T\sim$300 K (see inset to Fig. 3f). We find that σ_{MS} increases monotonically with V_G, indicating n-type behaviour, an on-off ratio of ≈ 25 (maximum gate-induced modulation of $\approx 2500\%$), and a mobility of up to $\approx 10^{-1}$ cm^{2}V^{-1}s^{-1}, in line with our recent results [134]. Below $T\sim$300 K the response of σ_{MS} to the dielectric gating proved weak and we consequently resorted to ionic gating to tune σ_{MS} at low T by scanning V_G in 0.125 V steps between 0 and +2 V. At each step, a waiting time of $\sim$10 min minimised the influence of diffusion dynamics of the ions inside the MoS_2 film. We recorded the T dependence of σ_{MS} between 300 and 220 K, below which the channel integrity was compromised by the freezing of the ionic liquid. As shown in Fig. 3f, at $T\sim$300 K the ionic-gate induced modulation of σ_{MS} exhibits n-type behaviour with an on-off ratio of ≈ 50, twice the one induced by the solid-oxide gate, and which increases to ≈ 85 as T is lowered to 220 K. Notably, we find that for $V_G \lesssim 1.37$ V, σ_{MS} increases upon increasing T, similar to the ungated case shown in Fig. 3c, whereas an opposite dependence of σ_{MS} is observed for $V_G \gtrsim 1.37$ V. This suggests that, above 220 K, a crossover from a hopping transport over localized states to a band-like transport over extended states can be induced in the printed MoS_2 devices by field effect.

The nearly linear scaling of σ with V_G for both the graphene and MXene printed devices (see also Fig. S8) at any T for $|V_G| \leq 40$ V, allows us to determine the field-effect mobility μ_{FE} in both devices (see Methods). The T-dependencies of μ_{FE} (Fig. 3g) are opposite between the printed graphene device ($\mu_{FE,GR}$, red squares) and the printed MXene device ($\mu_{FE,MX}$, green diamonds): $\mu_{FE,GR}$ decreases from ~ 0.6 to ~ 0.2 cm^{2}V^{-1}s^{-1} when the device is cooled from $T\sim$290 K to 4 K, whereas $\mu_{FE,MX}$ slightly increases from ~ 0.4 to ~ 0.5 cm^{2}V^{-1}s^{-1} in the same T range. The values of $\mu_{FE,MX}$ are in good agreement with those reported both in single-layer MXene FETs ($0.6 - 2.6$ cm^{2}V^{-1}s^{-1}) [54, 55] and in thicker MXene films obtained by spin-casting and interfacial film formation ($0.9 - 1$ cm^{2}V^{-1}s^{-1}) [56, 57]. The weak increase of $\mu_{FE,MX}$ as T decreases is typical of disordered metallic systems where the main source of charge-carrier scattering comes from defects [60, 61]. On the other hand, the values of $\mu_{FE,GR}$ are lower than those earlier reported for inkjet-printed graphene FETs on PET [3]. A possible reason for this discrepancy may lie in the more regular arrangement of the flakes in the printed graphene films on PET substrate [3] with respect to our films printed on SiO_2, as discussed in the next section. This correlation with the morphology of the system is reasonable since, as already mentioned, the conduction in the graphene films is clearly dominated by inter-flake resistance. The monotonic increase of $\mu_{FE,GR}$ with increasing T below 200 K is the expected behavior when the charge transport occurs via hopping processes [35, 137, 138]. Similarly, the saturation and slight decrease of $\mu_{FE,GR}$ between $T \sim$ 200 K and 290 K are consistent with a non-negligible impact of e-ph scattering in this higher T range [35, 45–47].

In the printed MoS_2 devices, two clearly different slopes in the plot of σ_{MS} as a function of V_G can be observed in the hopping and band-like conduction regions above and below $V_G \approx 1.37$ V. We thus determine $\mu_{FE,MS}$ in the temperature range from $T\sim$300 K to $T\sim$220 K for these two cases separately, resulting in $\mu_{FE,MS}$ slightly decreasing from $\sim$0.034 to $\sim$0.032 cm^{2}V^{-1}s^{-1} for $V_G \lesssim 1.37$ V (hollow blue circles in Fig. 3g), and $\mu_{FE,MS}$ increasing from $\sim$0.049 to $\sim$0.072 cm^{2}V^{-1}s^{-1}, for $V_G \gtrsim 1.37$ V (filled blue circles). These values result in agreement with the $\mu_{FE,MS}$ recently reported for inkjet-printed MoS_2 FETs [134]. The opposite T-dependencies exhibited by $\mu_{FE,MS}$ above and below $V_G \approx 1.37$ V are obviously consistent with a crossover from hopping transport at low V_G to a band-like one at high V_G, similar to the behavior reported in disordered isolated MoS_2 flakes [35]. The values of $\mu_{FE,MS}$ in our ion-gated devices are also consistent with both those determined in the same devices in the absence of the ionic liquid (up to $\approx 10^{-1}$ cm^{2}V^{-1}s^{-1}) and with those of ion-gated MoS_2 networks reported in the literature ($10^{-2} - 0.1$ cm^{2}V^{-1}s^{-1}) [4, 85]. In the next sections, we will show that these indications are confirmed by a more refined analysis of the temperature dependence of the conductivity.

The intrinsic carrier density $n_{3D}|_0$, calculated by using the field-effect mobility (see Methods), is plotted as a function of temperature in the inset to Fig. 3g, for both the printed graphene device ($n_{3D}|_{0,GR}$, red squares) and the printed MXene device ($n_{3D}|_{0,MX}$, green diamonds). We note that $n_{3D}|_{0,MX}$ remains $\sim 3 \cdot 10^{21}$ cm^{-3} at all temperatures, which falls within the reported range for both MXene flakes and films ($2 - 30 \cdot 10^{21}$ cm^{-3}) [54–57]. This behaviour is also typically observed in normal metals [64]. In the printed graphene device, on the other hand, $n_{3D}|_{0,GR}$ is smaller than $n_{3D}|_{0,MX}$ by over two orders of magnitude and decreases weakly from 10 to $6 \cdot 10^{18}$ cm^{-3} upon decreasing of T from 290 K to 4 K, a feature commonly observed in disordered systems where the charge transport occurs via hopping processes [60, 61]. Considering the average flake thickness $t_{av,GR} \sim$ 6.5 nm, these values correspond to an average intrinsic density of free carriers per graphene flake

ranging between ~ 4 and $\sim 7 \cdot 10^{12}$ cm^{-2}, which are typical values found in air-exposed graphene [34, 135] and graphene inks [21]. We also note that the values of the intrinsic carrier density at low temperature are consistent with those determined via the Hall effect at 4.2 K in both materials (see Supplementary Information and Fig. S9), i.e $n_{\mathrm{H,MX}} = 2.3 \pm 0.7 \cdot 10^{21}$ cm^{-3} and $n_{\mathrm{H,GR}} = 8.1 \pm 2.6 \cdot 10^{18}$ cm^{-3}.

A. Hopping transport in inkjet-printed MoS_2 devices

To gain further insights into the conduction mechanism of the inkjet-printed MoS_2 devices, we now consider in more detail the scaling of σ as a function of T. In this analysis, we will make use of robust models originally developed for disordered crystalline materials, and lately validated for various granular systems including 2D material networks [82–86]. In our picture of the charge transport, structural parameters like flake size and thickness, degree of overlap and flake orientation, are expected to be of primary importance in the description of granular systems, mainly affecting the absolute value of the conductivity, rather than its temperature dependence, on which our analysis will be focused. In general, the electrical conductivity in any hopping regime shows a temperature dependence of the type [35, 42, 60, 61, 73, 91]:

$$\sigma(T) = \sigma_0 \exp\left[-\left(\frac{T_0}{T}\right)^p\right] \qquad (1)$$

where T_0 is a characteristic temperature, σ_0 is the conductivity for $T \to \infty$ and p is an exponent which depends on the specific type of hopping mechanism. In the NNH mechanism, p is equal to 1 and σ follows a simple activated behavior with an activation energy $E_a = k_B T_0$ [60, 61], k_B being the Boltzmann constant. On the other hand, all VRH mechanisms exhibit $p < 1$, with the Efros-Shklovskii VRH mechanism (ES-VRH) being characterised by $p = 1/2$ (meaning that a soft gap is opened in the DOS at the Fermi level [60, 61, 73]) and the Mott-VRH mechanism exhibiting $p = 1/(1+d)$, where d is the dimensionality of the system [60, 61, 73].

Fig. 4a shows σ as a function of $T^{-1/4}$ in a representative printed MoS_2 device (blue solid line and hollow circles) in the absence of a gate voltage (ungated). It can be seen that, when plotted in logarithmic scale, σ scales linearly with $T^{-1/4}$ for $T \lesssim 200$ K (i.e. $T^{-1/4} \gtrsim 0.26\,\mathrm{K}^{-1/4}$, unshaded region in Fig. 4a), which is indicative of 3D-Mott VRH conduction [35, 42, 60, 61, 73, 91]. A fit of the curve in this temperature range to Eq. 1 with $p = 1/4$ gives $T_{0,\mathrm{MS}} = (3.07 \pm 0.10) \cdot 10^6$ K, which is one order of magnitude larger than the T_0 reported in ungated individual MoS_2 nanoflakes [35, 42] indicating that our MoS_2 device is more insulating than individual disordered MoS_2 flakes.

To further confirm that the charge transport at $T \lesssim 200$ K occurs through 3D Mott-VRH, we determine in a more accurate way the scaling factor p starting from the reduced activation energy W, defined as [91, 92]:

$$W(T) = \frac{\partial(\ln(\sigma))}{\partial(\ln(T))}. \qquad (2)$$

The scaling factor p is the slope of the linear fit of $\ln(W)$ as a function of $\ln(T)$ [92]. The values of $\ln(W)$ for our

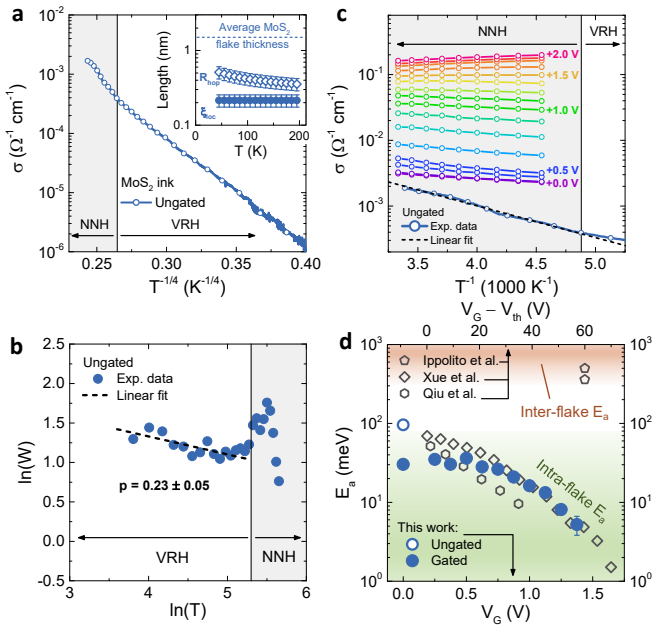

FIG. 4. **a**, Conductivity σ as a function of $T^{-1/4}$ for a printed ungated MoS_2 device (blue solid line). Hollow symbols indicate the data points used to determine the reduced activation energy W shown in **b**. The grey shaded region highlights the T range ($T \gtrsim 200$ K) where σ deviates from the $T^{-1/4}$ scaling due to the onset of NNH conduction. Inset: localization length ξ_{loc} (filled circles) and average hopping distance R_{hop} (hollow diamonds) as a function of T. The lengths are obtained combining the T-dependence of σ with the estimated values of $N(E_F)$ using Eq. 3. The horizontal dashed line highlights the average flake thickness in the MoS_2 ink. **b**, $\ln(W)$ as a function of $\ln(T)$ extracted from the numerical derivation of the data shown in panel **a**. The dashed black line is the linear fit to the data in the range $\ln(T) \leq 5$, which allows determining the corresponding value of the scaling exponent p. **c**, σ as a function of the inverse temperature T^{-1}, for different values of the gate voltage V_G. The circles indicate the points used to determine the transfer curves in Fig. 3f. The blue curve refers to the ungated device, and the dashed black line is the linear fit to these data for $T \geq 200$ K, i.e. in the NNH regime (grey-shaded region). **d**, Activation energy E_a as a function of V_G (bottom scale) in different MoS_2 devices. Blue circles circles are obtained from the fit of the conductance curves of panel **c**. Black symbols are the values of E_a reported in disordered MoS_2 flakes (from Ref. 35, diamonds and Ref. 42, hexagons) and in MoS_2 networks (from Ref. 85, pentagons) as a function of the difference between the solid-gate voltage and the threshold voltage for electronic conduction (top scale).

inkjet-printed MoS_2 devices are reported as a function of $\ln(T)$ in Fig. 4b, and their linear fit in the region $\ln(T) \lesssim 5.3$ (dashed line) gives $p_{MS} = 0.23 \pm 0.05$, in good agreement with the expected $p = 1/4$ for a 3D Mott-VRH mechanism.

Above 200 K, the scaling of $\ln(W)$ with $\ln(T)$ changes. On increasing T, the $\ln(W)$ shows a peak and then decreases faster than below 200 K, leading to $p_{MS} \geq 1$, which suggests the onset of a different transport mechanism. For $T \gtrsim 200$ K (grey-shaded region in Fig. 4a), $\ln(\sigma)$ scales with the inverse of the temperature, as highlighted in Fig. 4c where the same conductance (blue curve) is plotted as a function of T^{-1}. This fact indicates that at $T \gtrsim 200$ K the electric conduction occurs via the NNH mechanism [35, 42, 60, 61, 91]. Similar crossovers from Mott-VRH at low T to NNH at high T have been reported in disordered MoS_2 flakes [35, 42], although the VRH mechanism was invariably of the 2D-Mott type [35, 41, 42, 91]. By fitting the conductivity in the NNH region to Eq. 1 with $p = 1$ (dashed line in Fig. 4c) we find $E_{a,MS} = 96.1 \pm 0.5$ meV for our ungated printed MoS_2 device (blue hollow circle in Fig. 4d), which is comparable to the one reported for ungated individual MoS_2 nanoflakes [35, 42]. Fig. 4c also displays the conductance of the inkjet-printed MoS_2 for different values of V_G. Fitting these curves to Eq. 1 with $p = 1$ gives the activation energy as a function of the gate voltage shown in Fig. 4d (filled circles), which range between ~ 40 and ~ 4 meV. Note that a positive activation energy is obtained only from the fit of the curves up to $V_G = 1.37$ V, since for larger values of V_G, σ decreases with increasing T and a negative E_a is obtained, again consistent with the charge transport occurring over extended states for $V_G \gtrsim 1.37$ V and $T \gtrsim 200$ K. These findings indicate that, in the printed MoS_2 devices, the dominant charge transport mechanism crosses over from 3D-Mott VRH at low $T \lesssim 200$ K to NNH at high $T \gtrsim 200$ K. In any case, the VRH mechanism in our inkjet-printed MoS_2 devices differs from that expected for ES-VRH, characterized by a $T^{-1/2}$ scaling of $\ln(\sigma)$ (see Fig. S10).

We also try to understand whether the conduction of our devices is dominated by intra-flake or inter-flake hopping mechanisms. First of all, we note that the values of E_a extracted from the fit of the conductance curves in the NNH regime, in both our ungated and gated devices (hollow and filled blue circles in Fig. 4d respectively), are comparable to those obtained in disordered, isolated MoS_2 flakes [35, 42] rather than to the much larger ones obtained in MoS_2 networks [85] where the conduction is dominated by inter-flake hopping. Then, we calculate the characteristic localization length ξ_{loc} and the average hopping distance R_{hop} in the VRH regime and compare them with the typical size of the flakes. ξ_{loc} is directly related to the characteristic temperature T_0, and for 3D-Mott VRH the relationship is [60, 61]:

$$T_0 = \frac{24}{\pi k_B N(E_F) \xi_{loc}^3} \tag{3}$$

where $N(E_F)$ is DOS at the Fermi level E_F. Once ξ_{loc} is known, R_{hop} is simply [60, 139]:

$$R_{hop} = \frac{3}{8} \left(\frac{T_0}{T}\right)^{\frac{1}{4}} \xi_{loc} \, F_0 \tag{4}$$

where F_0 is a correction factor that describes the VRH regimes when the condition $T \ll T_0$ is not satisfied (see Fig. S11a). From the fit of the curve in Fig. 4a to Eq. 1 with $p = 1/4$, we obtain $T \ll T_{0,MS} = (3.07 \pm 0.10) \cdot 10^6$ K for our ungated printed MoS_2 device, resulting in $F_0 = 1$. $N(E_F)_{MS}$ can then be obtained from $E_{a,MS}$ in the NNH regime at $V_G = 0$ ($E_{a,MS} = 96.1 \pm 0.5$ meV), since $E_a^{-1} = N(E_F)a^3$ [60] where a is the minimum distance between hopping sites. From a statistics of the Raman spectra of the printed MoS_2 flakes (see Fig. S12), we determine the inter-defect length L_D and thus set $a = L_D \approx 1.54$ nm, in good agreement with previous reports ($a \approx 1.7$ nm [42]). We thus obtain $\xi_{loc,MS} = 0.21 \pm 0.04$ nm. This value is smaller than those found in ungated individual MoS_2 flakes, which range between 0.6 and 3.4 nm [35, 42, 91], and is consistent with the stronger insulating behavior exhibited by our printed MoS_2 devices.

The resulting values of the average hopping distance R_{hop} are plotted as a function of temperature in the inset to Fig. 4a as hollow diamonds, together with ξ_{loc} (filled circles). The horizontal line represents the average thickness of the MoS_2 flakes, $t_{av,MS}$. It turns out that $R_{hop,MS}$ ranges from about 0.3 nm (at $T = 200$ K) to about 0.5 nm (at $T = 45$ K) thus remaining smaller than $t_{av,MS}$ in the entire T range. This indicates that, on average, an electron will hop multiple times before being able to escape each MoS_2 flake in the out-of-plane direction, accounting for how a 3D VRH can be observed even when the flakes are quasi-2D and the rate-limiting step is *intra*-flake hopping, consistent with the observed values of E_a. This picture is in agreement with the observed distribution of flake orientations in the MoS_2 device (see Supplementary Information and Fig. S13), that demonstrates a fairly good alignment to the SiO_2 substrate, with a small average relative inclination of $\theta_{MS} < 3°$. This, together with the rather large lateral size of the flakes and their small average thickness, suggests an inkjet-printed film with high degree of alignment between the MoS_2 flakes with a good inter-flake connectivity in which, however, the conductivity is dominated by an intra-flake mechanism of conduction.

In conclusion, the charge transport in our inkjet-printed MoS_2 devices appears to be dominated by intra-flake hopping processes. Ungated devices sit deep in the insulating side of the IMT, and exhibit a crossover from 3D-Mott VRH conduction for $T \lesssim 200$ K to NNH conduction for $T \gtrsim 200$ K. Gated devices, on the other hand, exhibit NNH conduction for $T \gtrsim 200$ K up to $V_G \approx 1.37$ V, and an incipient crossover to a high-T conduction over extended states for larger values of V_G.

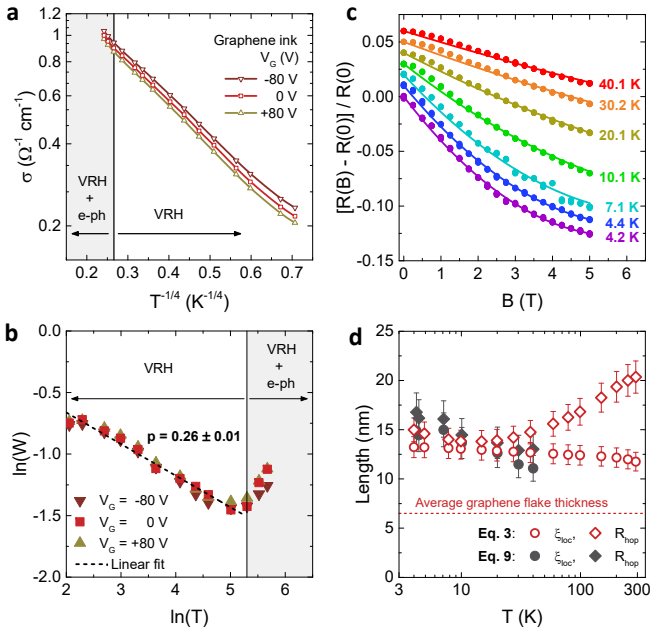

FIG. 5. **a**, Conductivity σ as a function of $T^{-1/4}$ curves for a printed graphene device at $V_G = -80$ V (brown solid line and hollow down triangles), $V_G = 0$ V (red solid line and hollow squares) and $V_G = +80$ V (yellow solid line and hollow up triangles). Hollow symbols are the data points used to determine the reduced activation energy W shown in **b**. The grey shaded region highlights the T range where a non-negligible contribution from e-ph scattering is present. **b**, $\ln(W)$ as a function of $\ln(T)$ extracted from the numerical derivation of the data shown in panel **a**. The dashed black line is the linear fit to the data in the range $2 \leq \ln(T) \leq 5$, which allows determining the corresponding values of the scaling exponent p. **c**, Magnetoresistance ratio $[R(B) - R(0)]/R(0)$ as a function of the magnetic field B at different temperatures. Filled circles are the experimental data, solid lines are the fits according to Eq. 9. Curves at different T are vertically offset by 0.01 for clarity. **d**, Localization length ξ_{loc} (circles) and average hopping distance R_{hop} (diamonds) as a function of T in the printed graphene device. The lengths indicated with red hollow symbols are obtained combining the T-dependence of σ with the estimated values of $N(E_F)$ using Eq. 3; those indicated by black filled symbols are instead obtained combining the T-dependence of σ with the MR fits of panel **c** using Eq. 9. The horizontal line highlights the average flake thickness in the graphene ink.

B. Hopping transport in inkjet-printed graphene devices

As already pointed out, the increase of conductance with T of the inkjet printed graphene device is qualitatively different from that of single graphene flakes; this alone suggests that the bottleneck for electric transport is interflake hopping. The conductivity σ of a representative inkjet-printed graphene device is reported in logarithmic scale in Fig. 5a, as a function of $T^{-1/4}$ and for three values of the back-gate voltage, i.e. $V_G = -80$ V (brown solid line and hollow down triangles), $V_G = 0$ V (red solid line and hollow squares), and $V_G = +80$ V (yellow solid line and hollow up triangles).

It can be seen that $\ln(\sigma)$ scales linearly with $T^{-1/4}$ for all values of V_G and up to $T \sim 290$ K, meaning that a 3D-Mott VRH conduction mechanism [35, 42, 60, 61, 73, 91] is at play over the entire T range. From the fit of the curves to Eq. 1 with $p = 1/4$, we obtain $T_{0,GR} = 138 \pm 11$ K, which is smaller than room temperature. This is commonly observed in networks composed of metallic grains when the charge transport is dominated by insulating inter-grain hopping [73, 76–82], and indicates that the printed graphene device is very close to the IMT [140, 141]. Indeed, in granular systems the inter-grain energy barrier is set by the presence of a finite inter-grain capacitance, and VRH behavior can be observed when electrostatic disorder lifts the Coulomb blockade and leads to a finite DOS at the Fermi level [73]. Notably, as shown in Fig. S10, the temperature dependence of $\ln(\sigma)$ is incompatible with a $T^{-1/2}$ scaling. Therefore, the 3D-Mott VRH mechanism observed in our devices differs from the hopping behavior reported in defective graphene (falling either in the ES-VRH regime [95] or in the 2D-Mott VRH regime [87, 88, 94]), but also from the metallic behavior usually exhibited by crystalline single- and few-layer graphene flakes [43–49], and from the hopping behavior observed in inkjet-printed graphene/polymer composites (NNH dominated by inter-flake capacitive charging) [86, 142] and spin-coated reduced graphene oxide (ES-VRH) [84].

Also in this case, we determine the scaling factor p through the calculation of the reduced activation energy W (Eq. 2) whose logarithm is plotted in Fig. 5b as a function of $\ln(T)$, for $V_G = 0, \pm 80$ V. Clearly, the behaviour is not monotonic and it displays a slope change at $\ln(T) \sim 5.3$ that corresponds to $T \sim 200$ K. A linear fit (black dashed line) to the curves $\ln(W)$ as a function of $\ln(T)$ in the range $2 \leq \ln(T) \leq 5$ provides the value of p in the VRH regime, that turns out to be $p_{GR} = 0.26 \pm 0.01$ irrespective of V_G. Above 200 K, i.e. $\ln(T) \geq 5.3$, W_{GR} increases with increasing T, indicating that the charge transport deviates from the expected scaling attributed to pure VRH, as already suggested the fact that $\mu_{FE,GR}$ decreases with T in the same T range (Fig. 3f). We identify $T \gtrsim 200$ K as the range of T where σ is no longer limited purely by the carrier hopping probability and a non-negligible contribution from electron-phonon scattering emerges in the printed graphene devices [45–47].

Interestingly, the dimensionality of the VRH scaling in the printed graphene devices is affected by the flake orientation. We find that the devices printed on SiO_2, which display a 3D-VRH, are characterized by a rather large average relative inclination of the flakes with respect to the substrate ($\approx 14°$, see Supplementary Information and Fig. S13). Instead, flexible inkjet-printed graphene films on PET exhibit a 2D-Mott VRH charge transport with $p_{GR} = 0.38 \pm 0.02$ (see Fig. S14) and, as evidenced by cross-sectional TEM analysis (see Fig. S15) have a

more pronounced in-plane orientation of the flake stacking. This suggests that it is the geometry of the printed flake network that sets the dimensionality of the VRH processes, meaning that inter-flake hopping is the mechanism that dominates the conduction of inkjet-printed graphene devices.

As a further test of this picture, we calculated $\xi_{\rm loc}$ and $R_{\rm hop}$ using Eqs. 3 and 4. Since the printed graphene devices do not exhibit NNH behavior in any temperature range, $N(E_{\rm F})_{\rm GR}$ cannot be estimated by starting from the activation energy of NNH; rather, one can start from the average free carrier density per unit volume $n_{\rm 3D}|_{0,\rm GR}$ (see Methods) shown in the inset to Fig. 3g. The final result is that the localization length turns out to be $\xi_{\rm loc,GR} \sim 13$ nm (hollow red circles in Fig. 5d). The values of $R_{\rm hop}$, calculated by using Eq. 4, are reported as a function of temperature in the same figure (hollow red diamonds). $R_{\rm hop,GR}$ shows a non-monotonic temperature dependence. At the lowest temperatures ($T < 40$ K) it slightly decreases with increasing T, going from $R_{\rm hop,GR} \sim 16$ nm to $R_{\rm hop,GR} \sim 13$ nm; for $T > 40$ K instead it slowly increases, reaching $R_{\rm hop,GR} \sim 20$ nm close to room temperature. This behavior can be ascribed to the fact that, in this case, $T_{0,\rm GR} = 138 \pm 11$ K is smaller than room temperature and the factor F_0 in Eq. 4 becomes relevant as T approaches and exceeds $T_{0,\rm GR}$. Finally, and most importantly, in the printed graphene devices $R_{\rm hop,GR}$ is systematically larger than the average flake thickness $t_{\rm av,GR}$ for any T, which is consistent with the carrier hopping in the inkjet printed graphene film occuring primarily between different flakes in the 3D network.

These results can be confirmed by investigating the magnetoresistance of our printed graphene devices (the magnetic-field dependence of the resistivity $\rho = \sigma^{-1}$), since measuring the magnetoresistance of a material in the VRH regime allows directly probing $\xi_{\rm loc}$ without having to make any assumption on its DOS [139, 143, 144]. In particular, in the case of 3D-Mott VRH and in the low magnetic field limit ($B \ll B_{\rm sat}, B_{\rm c}$) the magnetoresistance ratio MR $= [\rho(B) - \rho(0)]/\rho(0)$ takes a specific field dependence given by Eq. 9, containing $\xi_{\rm loc}$ as a parameter (see Methods). Fig. 5c shows the experimental values of MR as a function of B (symbols), measured with magnetic fields in the out-of-plane direction. Different colors refer to different temperatures between 4.2 K and 40.1 K, and the datasets at different T are vertically offset by 0.01 for clarity. The solid lines in the same figure represent the best fit to our experimental MR data using Eq. 9. The MR is always negative, quasi-linear at low B, with an incipient saturation at high B for $T \leq 20$ K. Such a behavior is typical of the magnetoresistance in the VRH regime, which is determined by the sum of a linear ($\propto B$) and a quadratic ($\propto B^2$) contribution [139, 143, 144] arising from the quantum interference of different hopping paths [143, 145] and the contraction of the charge-carrier wavefunction at impurity centers [143, 146], respectively. Our fits with this model show an excellent agreement with the experimental data. In Fig. 5d we plot the values of $\xi_{\rm loc,GR}$ (filled black circles) and $R_{\rm hop,GR}$ (filled black diamonds) obtained from the best fits of the MR data in Fig. 5c (further details in Methods). Both $\xi_{\rm loc,GR}$ and $R_{\rm hop,GR}$ are ~ 15 nm at 4.3 K and decrease to ~ 11 nm and ~ 13 nm at 40.1 K respectively, in excellent agreement with the values determined from the estimation of $N(E_F)_{\rm GR}$ (hollow red circles and diamonds, respectively).

Overall, we conclude that the charge transport in our printed graphene devices as a function of both T and B can be fully described in terms of a Mott VRH conduction dominated by inter-flake hopping processes, and on the verge of an IMT for $T \geq T_{0,\rm GR}$.

C. Weakly-localized transport in printed MXene devices

We now investigate the charge transport properties of the inkjet-printed MXene field-effect devices. In Fig. 6a we show the resistivity as a function of T of a printed MXene device of thickness $t_{\rm d,MX} \sim 30$ nm (solid green line, left scale) and compare it to that of a 28-nm-thick MXene film epitaxially grown on sapphire, as reported in Ref. 53 (filled black diamonds and solid black line, right scale). We immediately observe that, despite the comparable thickness, the ρ of the printed film is about one order of magnitude larger than that of the epitaxial film (at $T = 290$ K, $\rho = 47.6$ and 5.86 $\mu\Omega$ m respectively), which suggests that the printed film is more disordered than the epitaxial film, as expected. In both cases ρ depends only weakly on T, in full contrast with the exponential dependence observed in the printed graphene and MoS_2 films, and in line with the typical behavior of a disordered metallic system [60, 61, 74, 75]. In the printed MXene film for $T \geq 100$ K, ρ increases with increasing T, which is a fingerprint of conduction occurring over extended states [60, 61, 74, 75] when e-ph scattering is activated by the increasing T [64]. For $T \leq 100$ K, on the other hand, ρ exhibits an upturn, i.e. it reaches a minimum at $T \sim 80$ K and increases again with decreasing T (Fig. 6a). Such a low-T behaviour is typical of disordered 2D metals [65, 147]. Interestingly, the same trend was observed in isolated Ti_3C_2 MXene flakes [54], epitaxial films [53] and spray-casted networks [83], strongly pointing to a common charge transport mechanism in all these systems. To note, the inkjet-printed MXene film with a $t_{\rm d,MX} \sim 30$ nm shows an excellent substrate conformality, with a narrow distribution of the average relative inclination of the flakes peaked at $\theta_{\rm max,MX} \sim 0.63°$ (see Supplementary Information and Fig. S13). This, together with the large lateral size ($\langle S \rangle_{\rm MX} \sim 700$ nm) and small thickness ($t_{\rm av,MX} \sim 3.5$ nm) of the flakes makes the possibility of a mainly 2D charge transport rather reasonable.

To get further insights on the ρ upturn – observed for $T \leq 80$ K in Fig. 6b – we investigate the dependencies

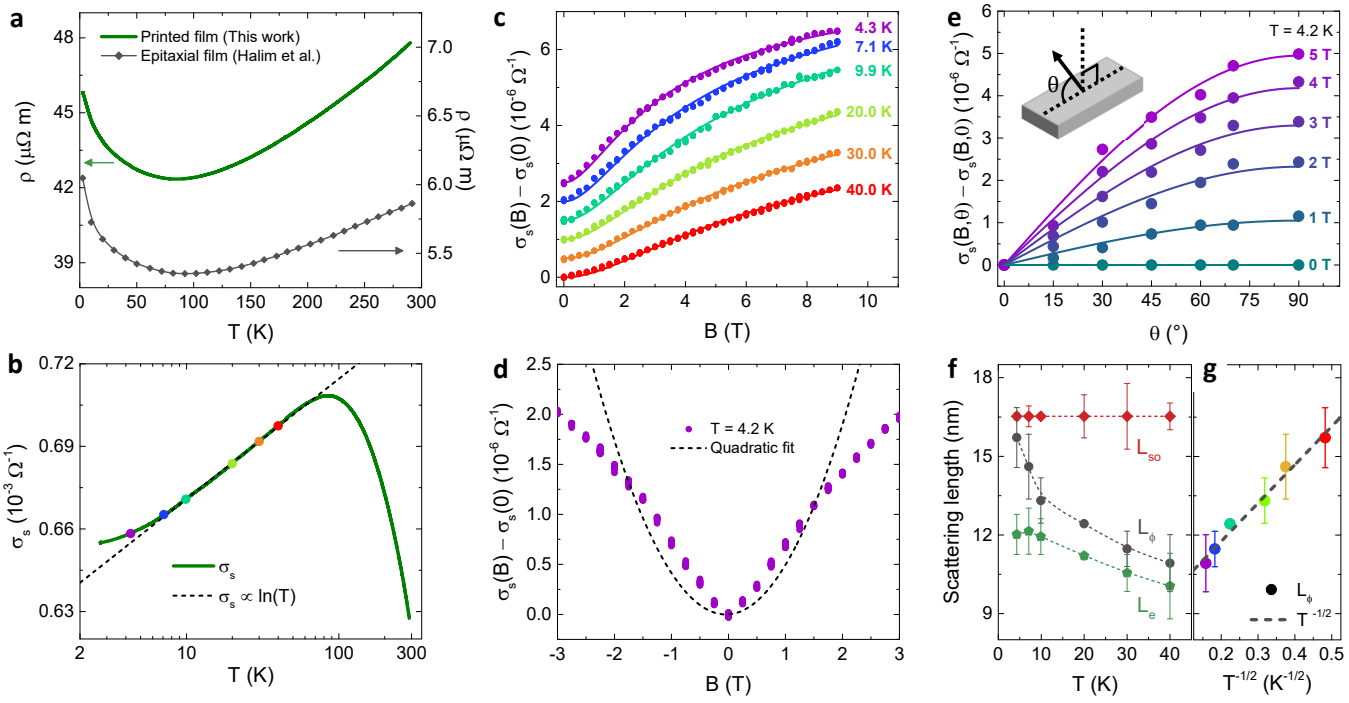

FIG. 6. **a**, Resistivity ρ as a function of T for a printed MXene device (solid green line, left scale) compared to that of an epitaxial MXene film from Ref. 53 (black solid line and filled diamonds, right scale). **b**, Same data of panel **a** for the printed MXene device, plotted as conductivity per unit surface σ_s as a function of $\log(T)$ (solid green line). The dashed black line is a linear fit to the data. Filled coloured circles mark the values of T at which the B sweeps shown in panel **c** were acquired. **c**, Magnetoconductance $\sigma_{2D}(B)$ - $\sigma_{2D}(0)$ as a function of the intensity B of the magnetic field (perpendicular to the film), for increasing temperatures. Filled circles are the experimental data, solid lines are the fits according to Eq. 12. Curves at different T are vertically shifted by $5 \cdot 10^{-7}\,\Omega^{-1}$ for clarity. **d**, $\sigma_{2D}(B)$ - $\sigma_{2D}(0)$ as a function of B (perpendicular to the film) for low positive and negative values of B. Violet circles are the experimental data at $T = 4.3$ K, the black dashed line is a quadratic fit to the data for $-2 \leq B \leq +2$ T. **e**, Anisotropic magnetoconductance as a function of the angle θ between B and the substrate plane, for different values of B. Filled circles are the experimental data at $T = 4.2$ K. Solid lines are fits to $\sin(\theta)$ dependencies. **f**, Spin-coherence length L_{so} (red diamonds), phase-coherence length L_ϕ (black circles) and elastic scattering length L_e (green pentagons) as a function of T, as determined from the fits to Eq. 12 shown in panel **c**. Dashed lines are guides to the eye. **g**, L_ϕ as a function of $T^{-1/2}$ (filled coloured circles) and a linear fit to the data (black dashed line).

of the conductivity per unit surface $\sigma_s = \sigma \cdot t_{d,MX}$ on T and B. Fig. 6b (solid green line; the filled coloured dots are the values of $\sigma_s(B = 0)$ obtained in the B-dependent measurements) shows σ_s as a function of T in semilogarithmic scale. The linear fit (black dashed line) shows $\sigma_s \propto \ln(T)$ in the range $7\,\text{K} \leq T \leq 70\,\text{K}$. Such a logarithmic dependence of σ_s on T is usually observed in disordered 2D conductors [65, 66], but can also occur in granular metals where the inter- and intra-grain conductances are comparable [73–75]. However, in the latter case the fully-metallic T-dependence we observe experimentally for $T \gtrsim 100$ K cannot develop [73–75]. Considering that the same behavior was observed in isolated flakes [54] and epitaxial films [53], we thus treat our printed MXene devices as granular 2D metals where the *intra*-grain conductance dominates. This is further corroborated by the positive ratio (η) of the proportional change of $d\rho/dT$ to the proportional change in ρ due to the gate-induced doping (see Fig. S16) [83]. The logarithmic scaling of σ_s with T can then be due to three distinct phenomena (or a combination thereof): Kondo effect [71], EEI [69, 70] and WL [67, 68]. Among these, in epitaxial MXene thin films WL has been proposed to be responsible for the upturn of ρ occurring at low T [53]. However, in general these phenomena cannot be distinguished on the basis of the T-dependence of σ_s alone, but they each feature a unique dependence of the magnetoconductance $\Delta\sigma(B,T) = \sigma_s(B,T) - \sigma_s(0,T)$ on B due to their distinct physical origin, as detailed in the Supplementary Information.

We identify the processes responsible for the ρ upturn at $T \leq 70$ K, by measuring the magnetoconductance as a function of B for different values of T between 4.3 K and 40 K, plotted as filled circles in Fig. 6c (data at different T are shifted by $5 \cdot 10^{-7}\,\Omega^{-1}$ for clarity). At any T, we observe a finite and positive $\Delta\sigma(B,T)$, ruling out the B-independent EEI as a major source for the ρ upturn [49, 66, 69, 70]. As shown in Fig. 6d,

$\Delta\sigma(B,T)$ is symmetric for positive and negative values of B, but even at $T = 4.2$ K (filled violet circles) does not follow a quadratic behavior in the low-field limit ($|B| \leq 2$ T) and cannot be fitted satisfactorily by a parabola (black dashed line), thus excluding Kondo effect as a source for the ρ upturn as well [72, 104]. We then determine the anisotropic magnetoconductance AMC $= \sigma_s(B,\theta) - \sigma_s(B,0)$, where θ is the angle between the applied magnetic field and the substrate plane. As shown in Fig. 6e, for all values of B the experimental AMC data (filled circles) closely follows the $\sin(\theta)$ dependence expected for a 2D Fermi surface [148] (solid lines), and the positive $\Delta\sigma(B,T)$ observed upon the application of an out-of-plane magnetic field ($\theta = 90°$) is entirely suppressed when the magnetic field is applied in-plane ($\theta = 0°$), as expected in the case of 2D WL behavior [65, 66] (see also Fig. S17). Consistently with the findings on epitaxial MXene films [53], we thus attribute the source of the ρ upturn below $T \lesssim 80$ K to the presence of 2D WL, and analyze quantitatively our data employing the Hikami-Larkin-Nagaoka (HLN) model [149, 150] (see details in Methods). The fits of the experimental $\Delta\sigma(B,T)$ values to Eq. 12 are reported as solid lines in Fig. 6c (the fitting curves are shifted by an identical amount to the corresponding experimental data sets). All the fiting functions are in agreement with the experimental values of $\Delta\sigma(B)$ for all values of T, which further corroborates the fact that the charge transport in our inkjet-printed MXene field-effect devices can be well described in terms of WL in the presence of a finite spin-orbit interaction (SOI) and that no qualitative differences are present with respect to the behavior of epitaxial thin films [53].

From the fits in Fig. 6c we can also determine the phase-coherence length L_ϕ, the spin-orbit length L_{so}, and the elastic-scattering length L_e in our printed MXene field-effect devices (Supplementary Information and Methods). Fig. 6f shows L_ϕ, L_{so} and L_e as red diamonds, black circles and green hexagons respectively, and the dashed lines act as guides to the eye. We find L_{so} to be constant with T, as typically observed in 2D conductors with finite SOI [151], and larger than both L_ϕ and L_e across the entire T range considered. This indicates that at any $T \geq 4.3$ K the SOI in the MXene flakes is unable to induce a complete spin precession in the charge carriers before they lose phase coherence, which would destroy the constructive interference responsible for WL and lead to the appearance of weak anti-localization (WAL). Indeed, no WAL-induced negative magnetoconductance close to $B = 0$ is observed in the experimental data in Fig. 6c,d, in agreement with the results on MXene epitaxial films [53]. On the other hand, we find that L_ϕ decreases upon increasing T, consistent with the fact that the phase-breaking inelastic scattering rate increases upon increasing T. Fig. 6g also shows that L_ϕ scales as $T^{-1/2}$, which identifies Nyquist electron-electron scattering as the main source of dephasing in the system [49, 151, 152]. The value L_e is found to be nearly T-independent for $T \leq 10$ K, as expected for elastic scattering with defects at low T, and weakly decreasing at larger T. Furthermore, the magnitude of $L_e \sim 10$ nm in our printed MXene device is comparable but larger than the mean free path ~ 2 nm estimated at 300 K from optical conductivity measurements in MXene films grown via the interfacial method [56], suggesting that e-ph scattering processes are responsible for the reduced mean free path observed at room T.

Finally, we focus on the behavior of σ_s as a function of T for $T \lesssim 7$ K. As shown in Fig. 6b, σ_s (solid green line) deviates from a perfect logarithmic scaling (black dashed line) in this T range and shows an incipient saturation for $T \leq 4$ K. Such a behavior can occur in weakly-localized granular materials either when L_ϕ is smaller than but comparable to L_{so}, allowing the SOI to reduce the constructive interference responsible for WL [151], or when L_ϕ approaches the lateral size of the metallic grains, resulting in *inter*-flake coherent charge transport [153, 154]. As shown in Fig. 6f, at $T = 4.3$ K L_ϕ is indeed approaching L_{so}, whereas L_ϕ, L_{so} and L_e remain much smaller than the average lateral size of the MXene flakes ($\langle S \rangle_{MX} = 710$ nm) at any T. Consequently, the deviation of σ_s from the logarithmic scaling can be ascribed to an incipient crossover to WAL due to the finite SOI, and the WL behavior in our printed MXene devices is fully determined by phase-coherent *intra*-flake charge transport.

V. CONCLUSIONS

We successfully unveiled the charge transport mechanisms of thin-film field-effect devices of semiconducting (MoS_2), semimetallic (graphene) and metallic (MXene) made from representative few-layer E2D inks, fabricated via direct inkjet-printing on SiO_2/Si substrates. We investigated their electrical conductivity as a function of temperature, magnetic field and gate voltage, accounting for morphological features of the flakes and the printed films. We demonstrated that the charge transport in the printed MoS_2 and MXene devices is dominated by the intrinsic *intra*-flake processes, leading to a temperature-induced crossover between 3D-Mott variable-range hopping and nearest-neighbor hopping in the former and a weakly-localized metallic behavior in the latter. In the printed graphene devices, we demonstrated that the charge transport is determined by *inter*-flake processes, leading to a variable-range hopping behavior up to room temperature in spite of the semimetallic nature of the single flakes, and resulting in a strong dependence of the dimensionality of the charge transport on that of the flake network in the printed film. Our findings establish the fundamental mechanisms responsible for charge transport in inkjet-printed devices made of E2D inks, and pave the way for a reliable design of more complex printed electronics with E2D inks.

METHODS

Ink Preparation

Graphene ink – The graphene inks was prepared by a surfactant-free liquid-phase exfoliation of graphite using a high-boiling-point solvent which was then solvent-exchanged into a low-boiling-point solvent, thus minimising solvent residuals. The use of a low-boiling-point solvents aids at preventing the coffee-ring effect hence creating a uniform film. In addition we used a low-boiling-point solvent which is non-toxic and does not damage the inkjet-printer cartridge (piezoelectric-based printhead) during the printing process. An initial 1.5 g of Sigma Aldrich (Sigma-Aldrich No. 332461, size $< 100\,\mu$m) graphite was added to 150 ml of NMP and ultrasonicated (Fisherbrand FB15069, Max power 800 W) for 9 hrs. The graphite-NMP ink was subsequently centrifugated (Sorvall WX100 mounting a TH-641 swinging bucket rotor) for 1 hr at 10,000 rpm. The supernatant was transferred into a clean glass bottle using a micropipette. Great care was taken during pipetting to avoid the disturbance of the sediment layer which could re-disperse into the supernatant. The solvent exchange was carried out via vacuum filtration, where 20 ml of graphene ink was passed through a PTFE membrane (Merck Millipore, 0.1 μm). Graphene collected on the PTFE membrane was transferred to a small vial along with 5 ml of pure ethanol. This was followed by 10 minutes of ultrasonication. Printing was carried out immediately after the ink preparation.

Ti_3C_2 ink (MXene) – The MXene ink was prepared by following the mild-exfoliation-route protocol for MAX phase powder (Ti_3AlC_2). This involves etching the Al atom in the MAX powder via the creation of in-situ hydrofluoric acid. As for the graphene ink we also opted for a solvent exchange route for the MXene ink by exchanging the high-boiling-point solvent to a benign low-boiling-point solvent. In a vented 40ml PTFE vessel, deionised water (5 ml) was added, followed by drop-wise addition of concentrated hydrochloric acid (15 ml, Sigma). To the resultant 9M HCl, LiF powder (1g, Sigma) was added, and the vessel was then immersed in a mineral oil bath at 35°C and using a magnetic PTFE stirrer bar for 10 minutes to fully dissolve the LiF and allow the temperature to stabilise. Ti_3AlC_2 MAX phase powder (1 g, Carbon-Ukraine ltd.) was then added in small additions to the vessel to avoid overheating of the solution. The solution was then left stirring for 24 hours to obtain the etched, multilayer $Ti_3C_2T_x$ MXene. The contents of the vessel were transferred into a 50 ml centrifuge tube and diluted to a total of 40 ml with deionised water. The dispersion was then sedimented via centrifugation at 5000 rpm using a Thermo Scientific Heraeus Multifuge X1 for 5 minutes, discarding the supernatant and repeating several times, until the pH of the supernatant was 6. To delaminate the washed multilayer MXene, the tube was sealed tightly and shaken vigorously by hand and vortex mixing for 30 minutes. The dispersion was then centrifuged at 1500 rpm for 30 minutes to sediment any many-layer MXene or unreacted MAX phase. The supernatant containing delaminated MXene flakes was then collected.

For ease of printing, the dispersion was transferred into NMP (Sigma Aldrich) via centrifugation at 5000 rpm, redispersing the sediments in minimal NMP and repeating three times to remove remaining water. To obtain a printable MXene dispersion in ethanol, the NMP ink was transferred via centrifugation, repeating 3 times with absolute ethanol (5 ml, Fisher Scientific). The resulting dispersion was sonicated for 15 minutes to break up agglomerated flakes and then centrifuged at 2500 rpm for 30 minutes to remove any remaining agglomerates. The supernatant was collected for use in inkjet printing.

MoS_2 ink – The MoS_2 ink was prepared by following the electrochemical exfoliation route which involved the intercalation of quaternary ammonium bromide in between the bulk MoS_2 layers. The electrochemical set up involved using a natural MoS_2 crystal (HQ graphene) and a graphite rod (Qingdao Tennry Carbon Co.) as the cathode and anode respectively. The electrolyte was made by adding 200 mg (0.2 g) of quaternary ammonium bromide (Sigma-Aldrich, CAS number: 4368-51-8, SKU: 87301) to 40 ml of acetonitrile giving a concentration of 5 mg ml^{-1}. Both the MoS_2 crystal and graphite electrode were submerged in the quaternary ammonium bromide electrolyte and the applied voltage was set at 8 V for 1 hr. The expanded MoS_2 crystal was washed with ethanol and then broken up into smaller pieces. The small pieces of MoS_2 were transferred to a test tube and Dimethylformamide (DMF) with Polyvinylpyrrolidone (PVP) (22 mg ml^{-1}, Sigma-Aldrich, CAS Number 9003-39-8, SKU: PVP40, Molecular weight 40,000) was added to the test tube and the mixture was sonicated for 30 minutes. The mixture was then broken down further using a shear mixer (IKA-T10). The dispersion was then centrifuged at 3000 rpm for 20 min to remove any large piece of MoS_2 that was not electrochemical exfoliated. The supernatant was then centrifuged again at 5000 rpm for 10 min to futher separate few-layer MoS_2 flakes from bulk MoS_2. Both centrifuge steps were preformed using a ProteomeLab™ XL-A by Beckman Coulter along with a SW 32 Ti Swing-Bucket rotor. The supernatant of the second centrifuge step was placed under a high vacuum line ($\sim$ 1 mbar) to remove the DMF solvent and concentrate the MoS_2 ink. The concentrate dispersion, which had a volume of 10 ml, was centrifuged at 45000 rpm for 30 min to sediment the MoS_2 flakes. This centrifuge step was preformed using a Beckman Optima MAX Ultracentrifuge. The sediment MoS_2 was re-dispersed in isopropyl alcohol (IPA) with PVP (22 mg ml^{-1}). The MoS_2 dispersed in IPA was directly used to print the MoS_2 film with no further processing required.

A. Transmission electron microscopy

Transmission electron microscopy (TEM) was performed using a FEI Philips Tecnai F-20 operated at 200 kV (Tungsten, LB6) with a line resolution of 0.10 and point resolution of 0.24 nm. The TEM sample were prepared by diluting the initial E2D ink by a factor of 100 and drop casting the diluted solution on holey carbon film 400 mesh copper (Cu) grid which was then allowed to dry in ambient air overnight.

B. Ink Jet printing

Before performing the printing process, each Si/SiO_2 substrate (Graphene supermarket 285 nm p-doped) was treated with ozone plasma (NanoBioAnalytics UV Ozone Cleaner UVC – 1014) to make the surface more hydrophilic. Drop on demand ink-jet printer (Fujifilm Dimatix DMP-2800) with a nozzle diameter of 21 μm that produce droplets with a volume of $\sim$ 10 pl was used to print the devices. The E2D inks were made using low-boiling-point solvents ($<$ 100°C) which evaporate at room temperature hence minimising both the transport of particulates (causing "coffee rings") and the redispersion of the material, thus improving the morphological uniformity of the film.

C. Rheology

A rotational rheometer (Discovery Hybrid Rheometer HR-1) that uses a parallel plate method to measure the viscosity and viscoelastic properties of a liquid was used to characterize all the inks employed in this work. Shear-thinning was observed in all the inks. The surface tension of the inks was measured using pendent drop method (First Ten Angstroms FTA1000B). Built in software analysed the shape of the suspended droplet formed at the end of the needle via drop shape analysis (DSA). Ink density (ρ) was measured by weighing 1 ml of ink on a microbalance (Sartorius ME5). The density of the inks was determined as ρ =m/V where m and V are the mass and volume respectively. All inks were formulated with surface tension (γ) $\sim$ 29 mN m^{-1} and viscosity (η) $\sim$ 1 mPa (see Figs. S6 and S7). The corresponding density of the inks is $\rho_{GR} \sim 0.8$ g cm^{-3}, $\rho_{MS} \sim 0.7$ g cm^{-3} and $\rho_{MX} \sim 0.99$ g cm^{-3} for the graphene, MoS_2 and MXene inks, respectively. The Ohnesorge number (a dimensionless number that relates the viscous forces to inertial and surface tension forces) is determined as $Oh = \mu/\sqrt{\rho\sigma L}$, where L is the diameter of the nozzle, and the corresponding figure of merit $Z = Oh^{-1}$ is derived.

D. Optical absorption spectroscopy

The flake concentration c of the graphene, MXene and MoS_2 inks was determined using the Beer-Lamber law $A = \alpha c l$, where c is the concentration, l is the beam path length and α is the absorption coefficient. For the latter, we used the values at 660 nm $\alpha_{660(GR)} \sim 2460$ L g^{-1} m^{-1} for the graphene ink [14], $\alpha_{660(MX)} \sim 538$ L g^{-1} m^{-1} for the MXene ink (see also Fig. S1) and $\alpha_{672(MoS_2)} \sim 3400$ L g^{-1} m^{-1} for the MoS_2 ink.

E. Raman spectroscopy

A Renishaw 1000 InVia micro-Raman spectrometer was used to acquire the Raman spectra. The spectra shown in Fig. 2 were measured using a 514 nm laser with an 20x objective. All the Raman spectra were acquired using $\sim$ 1 mW.

F. Atomic force microscopy

Inks were diluted by a factor of 100, then drop casted on pieces of Si/SiO_2 wafers and allowed to dry in ambient air. A short annealing step of 1 min at the boiling temperature of the solvent used to make the E2D ink, was performed before acquiring the AFM images. AFM measurements were performed using a Bruker Dimension icon with peakforce mode using a silicon tip on a Nitride lever.

G. X-ray photoelectron spectroscopy

Graphene ink and MoS_2 ink – A K-Alpha$^+$ surface analysis by Thermo Scientific was used to carry out measurements on all the inkjet printed devices on SiO_2. A spot size of $200 - 400\,\mu$m was used for all the samples. The spectra were obtained in vacuum at a pressure $< 8 \cdot 10^{-7}$ mbar. The system employs a microfocused Al Kα X-ray source (1486 eV) and a 2D detector attached to a 180 double-focusing hemispherical analyser. Further analysis of the XPS spectra was carried out using the Avantage software by Thermoscientific.

Ti_3C_2 ink – XPS spectra were recorded from an Omicron EA125 energy analyser (Scienta Omicron), using an XM1000 monochromated Al K X-ray source. The instrument's base pressure was $2 \cdot 10^{-10}$ mbar and the instrumental resolution was 0.6 eV. The spectra were deconvoluted and fitted using CasaXPS (Casa Software).

H. Device fabrication

All E2D ink devices were produced by using 25 printing passes. In the printed MoS_2 devices, we submerge

our devices in bis(trifluoromethane)sulfonimide (TFSI) in 1,2-dichloroethane at 100 °C for 1 h. The treatment is performed in a nitrogen glovebox to avoid exposing TFSI to moisture in ambient atmosphere [134, 155]. The devices are then annealed at 400 °C for 1 h to remove any residual solvent. We then created a thin gate oxide suitable for electric-field modulation. Electron-beam (e-beam) lithography was used to pattern ∼ 1 mm long source, drain and gate electrodes on Si/SiO_2 substrate. We use Ti/Au/(5/35 nm) for the source and drain and Al (40 nm) for gate electrode of the FET. A thin native AlO_x layer was formed at the top surface of Al by air exposure (the gate length is ∼ 600 nm and the width ∼ 400 μm).

I. Charge transport measurements

The electrical connections for charge transport measurements were realized by placing thin Au wires on the SiO_2/Si substrates close to the printed devices and then drop-casting small (∼ 100μm) droplets of electrically-conducting Ag paste (RS components). Temperature-dependent charge transport measurements were performed in the high-vacuum chamber of a Cryomech pulse-tube cryocooler with a base temperature of 2.8 K. Magnetic-field dependent measurements were performed in He atmosphere in the variable-temperature insert of an Oxford Instruments ^{4}He cryostat equipped with a 9 T superconducting magnet. The conductivity of the printed devices was determined as:

$$\sigma = \frac{l}{w t_{\rm d}} \frac{I}{V} \tag{5}$$

where l is the channel length, w its width, $t_{\rm d}$ is the device thickness, I the current flowing through the channel and V the voltage drop across it. The field-effect mobility was determined as:

$$\mu_{\rm FE} = \frac{t_{\rm d}}{C_{\rm G}} \left| \frac{\partial \sigma}{\partial_{\rm G}} \right| \tag{6}$$

and the average density of free carriers per unit volume at $V_{\rm G} = 0$, $n_{\rm 3D}|_0$, as:

$$n_{\rm 3D}|_0 = \frac{\sigma(V_{\rm G} = 0)}{e\ \mu_{\rm FE}} \tag{7}$$

where e is the elementary charge, $C_{\rm G} = \varepsilon_{\rm ox}\varepsilon_0/t_{\rm ox}$ is the gate capacitance per unit area, ε_0 is the vacuum permittivity, and $\varepsilon_{\rm ox}$ and $t_{\rm ox}$ are the dielectric constant and thickness of the gate oxide respectively. For the printed MXene and graphene devices, $t_{\rm ox}$ = 285 nm and $\varepsilon_{\rm ox}$ = 3.9 is the permittivity of SiO_2 [40], resulting in $C_{\rm G}$ = 12.1 nF cm^{-2}. For the printed MoS_2 devices, $t_{\rm ox} \approx$ 4 nm and $\varepsilon_{\rm ox} \approx$ 0.43 as an effective-medium approximation of AlO_x and vacuum, resulting in $C_{\rm G} \approx$ 98 nF cm^{-2} (see Ref. 134 for details.) For ion-gated MoS_2 devices, the same definition of $\mu_{\rm FE}$ is employed except that the solid-oxide capacitance is substituted for the ionic-gate capacitance $C_{\rm G}$≈10.8 μF cm^{-2} determined by low-bias cyclic voltammetry [4, 156] (see Supplementary Information and Fig. S18).

The printed MXene and graphene devices were measured in the four-probe configuration by supplying a small constant current $I_{\rm D} \sim 1\,\mu$A between the outer drain (D) and source (S) contacts with a two-channel Agilent B2912 source-measure unit (SMU), and measuring the longitudinal voltage drop $V_{\rm xx}$ between the inner voltage contacts with an Agilent 34420 nanovoltmeter. Common-mode offsets were removed by the current reversal method. The gate voltage $V_{\rm G}$ was applied between the S contact and the p-doped Si back gate with the same two-channel SMU. The printed MoS_2 devices were too resistive for the four-probe method to be reliable, and were thus measured in the two-probe configuration with a Keithley 2636B SMU by linearly sweeping $V_{\rm D}$ from −0.1 to +0.1 V, measuring the resulting $I_{\rm D}$, and performing a linear fit to the data. All the measured IV curves in the printed MoS_2 devices showed a linear behavior, indicating Ohmic contacts to the sample, and the contact resistance was determined to be negligible with respect to the total resistance of the device (see Fig. S19). In the printed MoS_2 devices in the absence of the ionic gate, an effective width w equal to 10% the apparent one was employed in the calculations, owing to the c-AFM measurements indicating that only a 10% fraction of the MoS_2 flakes were electrically connected to the Au leads.

J. Density of states of the graphene ink

We estimate $N(E_{\rm F})_{\rm GR}$ by combining the average free carrier density per unit volume $n_{\rm 3D}|_{0,\rm GR}$ (see Methods) shown in Fig. 3g, with the energy-dependence of the DOS in graphite as determined by *ab initio* density functional theory [157]:

$$n_{\rm 3D}|_0 = \int_{\rm E_D}^{\rm E_F} N(E) dE \tag{8}$$

where $E_{\rm D}$ is the energy of the Dirac point. We find that the resulting $\xi_{\rm loc,GR} \sim$ 13 nm is nearly independent on T, much larger than the one in the printed MoS_2 devices, and consistent with the more conductive behavior of the printed graphene devices.

K. Magnetoresistance and magnetoconductance fits

The magnetoresistance curves of the printed graphene device shown in Fig. 5e films were fitted to the standard expression for hopping transport [139, 143, 144]:

$$\mathrm{MR} = -C_{\rm sat} \frac{B}{B_{\rm sat}} + t^2 \frac{B^2}{B_{\rm c}^2} \tag{9}$$

Here, B_{sat} and B_c are characteristic values of B related to the localization length ξ_{loc}:

$$B_{sat} = 0.7 \left(\frac{8}{3}\right)^{\frac{3}{2}} \left(\frac{2\pi\hbar}{e\xi_{loc}^2}\right) \left(\frac{T}{T_0}\right)^{\frac{3}{8}} \quad (10)$$

$$B_c = \frac{6\hbar}{e\xi_{loc}^2} \left(\frac{T}{T_0}\right)^{\frac{3}{8}} \quad (11)$$

where C_{sat} is the positive saturation constant [143], $t^2 = 0.0893$ is a numerical coupling constant [143], and $\hbar$ is the reduced Planck constant. The corresponding values of B_{sat} and B_c were found to be always larger than 17 T and 8 T respectively, validating the choice of the low magnetic field limit.

Conversely, the magnetoconductance curves of the printed MXene device shown in Fig. 6 were fitted to the Hikami-Larkin-Nagaoka model, which describes the magnetoconductance of 2D metallic systems in presence of finite intrinsic SOI [151]:

$$\Delta\sigma(B) = \frac{e^2}{2\pi^2\hbar}\left[F\left(\frac{B_\phi}{B}\right)\right] + \frac{e^2}{2\pi^2\hbar}\left[F\left(\frac{B_{so}+B_e}{B}\right)\right] - \frac{3e^2}{2\pi^2\hbar}\left[F\left(\frac{(4/3)B_{so}+B_\phi}{B}\right)\right] \quad (12)$$

with

$$F(z) = \ln(z) - \psi(1/2+z) \quad (13)$$

and

$$B_{\phi,so,e} = \hbar/4eL_{\phi,so,e}^2 \quad (14)$$

where ψ is the digamma function [49].

The magnetic-field dependent charge transport data shown in Fig. 5e and Fig. 6e were fitted to Eq. 9 and Eq. 12, respectively, using a Levenberg-Marquardt algorithm as implemented in the OriginLab software. In both cases, the curve measured at the lowest T, being most sensitive to the fit parameters, was fitted first, and the uncertainties were determined automatically by the software. The best-fit parameters of the curve were then used as the initial guesses for the fit to the next curve at larger T, and the procedure was repeated at all values of T. At high T, the experimental curves were sometimes too smooth for the fits to converge, due to mutual dependency between the free parameters. In this case, multiple fits were performed fixing one parameter at a time while leaving the other parameters free. The final values of the parameters were then obtained by averaging the results, and the uncertainties determined by their maximum differences.

ACKNOWLEDGMENTS

The authors acknowledge funding from EPSRC grants EP/P02534X/2, EP/R511547/1, EP/T005106/1, the Imperial College Collaboration Kick-Starter grant, the MIUR PRIN-2017 program (Grant No.2017Z8TS5B – "Tuning and understanding Quantum phases in 2D materials – Quantum2D"), and the EU H2020 Graphene Flagship Core 3 Grant No. 881603. V.N. acknowledges the support of the ERC CoG grant 3D2DPrint and of the SFI Centres AMBER and IForm. A part of the electron microscopy characterization was carried out at the Advanced Microscopy Laboratory (AML) at the AMBER centre, CRANN Institute www.tcd.ie/crann/aml/, Trinity College Dublin, Ireland. AML is an Science Foundation Ireland (SFI) supported imaging and analysis centre. We acknowledge Mr Federico La Barbera (Universita' di Catania) for the support in the morphological analysis of the ink-jet printed devices.

[1] Torrisi, F. & Carey, T. Graphene, related two-dimensional crystals and hybrid systems for printed and wearable electronics. *Nano Today* **23**, 73–96 (2018).
[2] Torrisi, F. & Coleman, J. N. Electrifying inks with 2D materials. *Nat. Nanotechnol.* **9**, 738–739 (2014).
[3] Carey, T. *et al.* Fully inkjet-printed two-dimensional material field-effect heterojunctions for wearable and textile electronics. *Nat. Commun.* **8**, 1202 (2017).
[4] Kelly, A. G. *et al.* All-printed thin-film transistors from networks of liquid-exfoliated nanosheets. *Science* **356**, 69–73 (2017).
[5] Li, J., Naiini, M. M., Vaziri, S., Lemme, M. C. & Östling, M. Inkjet printing of MoS_2. *Adv. Funct. Mater.* **24**, 6524–531 (2014).
[6] Karagiannidis, P. G. *et al.* Microfluidization of graphite and formulation of graphene-based conductive inks. *ACS Nano* **11**, 2742–2755 (2017).
[7] Secor, E. B. *et al.* Gravure printing of graphene for large-area flexible electronics. *Adv. Mater.* **26**, 4533–4538 (2014).
[8] Ren, J. *et al.* Environmentally-friendly conductive cotton fabric as flexible strain sensor based on hot press reduced graphene oxide. *Carbon* **111**, 622–630 (2017).
[9] Qiang, S. *et al.* Wearable solid-state capacitors based on two-dimensional material all-textile heterostructures. *Nanoscale* **11**, 9912–9919 (2019).
[10] Parvez, K. *et al.* Exfoliation of graphite into graphene in aqueous solutions of inorganic salts. *J. Am. Chem. Soc.* **136**, 6083–6091 (2014).
[11] Lin, Z. *et al.* Solution-processable 2D semiconductors for high-performance large-area electronics. *Nature* **562**, 254–258 (2018).
[12] Su, C.-Y. *et al.* High-quality thin graphene films from fast electrochemical exfoliation. *ACS Nano* **5**, 2332–

2339 (2011).
[13] Paton, K. R. *et al.* Scalable production of large quantities of defect-free few-layer graphene by shear exfoliation in liquids. *Nat. Mater.* **13**, 624–630 (2014).
[14] Hernandez, Y. *et al.* High-yield production of graphene by liquid-phase exfoliation of graphite. *Nat. Nanotechnol.* **3**, 563–568 (2008).
[15] Hasan, T. *et al.* Solution-phase exfoliation of graphite for ultrafast photonics. *Phys. Stat. Sol. (B)* **247**, 2953–2957 (2010).
[16] Coleman, J. N. *et al.* Two-dimensional nanosheets produced by liquid exfoliation of layered materials. *Science* **331**, 568–571 (2011).
[17] Wen, D. *et al.* Inkjet printing transparent and conductive MXene ($Ti_3C_2T_x$) films: A strategy for flexible energy storage devices. *ACS Appl. Mater. Interfaces* **13**, 17766–17780 (2021).
[18] Zhang, C. J. *et al.* Additive-free MXene inks and direct printing of micro-supercapacitors. *Nat. Commun.* **10**, 1795 (2019).
[19] Finn, D. J. *et al.* Inkjet deposition of liquid-exfoliated graphene and MoS_2 nanosheets for printed device applications. *J. Mater. Chem. C* **2**, 925–932 (2014).
[20] Micallef, F. G. *et al.* Transparent conductors for mid-infrared liquid crystal spatial light modulators. *Thin Solid Films* **660**, 411–420 (2018).
[21] Bianchi, V. *et al.* Terahertz saturable absorbers from liquid phase exfoliation of graphite. *Nat. Commun.* **8**, 15763 (2017).
[22] Wang, F. *et al.* Graphene passively Q-switched two-micron fiber lasers. In *2012 Conference on Lasers and Electro-Optics (CLEO)*, 1–2 (IEEE, 2012).
[23] Jiang, X. *et al.* Inkjet-printed MXene micro-scale devices for integrated broadband ultrafast photonics. *npj 2D Materials and Applications* **3**, 34 (2019).
[24] Torrisi, F. *et al.* Inkjet-printed graphene electronics. *ACS Nano* **6**, 2992–3006 (2012).
[25] Kumar, D. K. *et al.* Scalable screen-printing manufacturing process for graphene oxide platinum free alternative counter electrodes in efficient dye sensitized solar cells. *FlatChem* **15**, 100105 (2019).
[26] Baker, J., Deganello, D., Gethin, D. T. & Watson, T. M. Flexographic printing of graphene nanoplatelet ink to replace platinum as counter electrode catalyst in flexible dye sensitised solar cell. *Mater. Res. Innov.* **18**, 86–90 (2014).
[27] Carey, T., Jones, C., Le Moal, F., Deganello, D. & Torrisi, F. Spray-coating thin films on three-dimensional surfaces for a semitransparent capacitive-touch device. *ACS Appl. Mater. Interfaces* **10**, 19948–19956 (2018).
[28] Sarycheva, A. *et al.* 2D titanium carbide (MXene) for wireless communication. *Sci. Adv.* **4**, eaau0920 (2018).
[29] Singh, M., Haverinen, H. M., Dhagat, P. & Jabbour, G. E. Inkjet printing – process and its applications. *Adv. Mater.* **22**, 673—685 (2010).
[30] McManus, D. *et al.* Water-based and biocompatible 2D crystal inks for all-inkjet-printed heterostructures. *Nat. Nanotechnol.* **12**, 343–350 (2017).
[31] Seo, J.-W. T. *et al.* Fully inkjet-printed, mechanically flexible MoS_2 nanosheet photodetectors. *ACS Appl. Mater. Interfaces* **11**, 5675–5681 (2019).
[32] Akinwande, D. Two-dimensional materials: printing functional atomic layers. *Nat. Nanotechnol.* **12**, 287–288 (2017).
[33] Ferrari, A. C. *et al.* Science and technology roadmap for graphene, related two-dimensional crystals, and hybrid systems. *Nanoscale* **7**, 4598–4810 (2015).
[34] Novoselov, K. S. *et al.* Electric field effect in atomically thin carbon films. *Science* **306**, 666–669 (2004).
[35] Xue, J., Huang, S., Wang, J.-Y. & Xu, H. Q. Mott variable-range hopping transport in a MoS_2 nanoflake. *RSC Adv.* **9**, 17885–17890 (2019).
[36] Ovchinnikov, D., Allain, A., Huang, Y.-S., Dumcenco, D. & Kis, A. Electrical transport properties of single-layer WS_2. *ACS Nano* **8**, 8174–8181 (2014).
[37] Baugher, B. W. H., Churchill, H. O. H., Yang, Y. & Jarillo-Herrero, P. Intrinsic electronic transport properties of high-quality monolayer and bilayer MoS_2. *Nano Lett.* **13**, 4212–4216 (2013).
[38] Radisavljevic, B. & Kis, A. Mobility engineering and a metal-insulator transition in monolayer MoS_2. *Nat. Mater.* **12**, 815–820 (2013).
[39] Park, M. J., Yi, S.-G., Kim, J. H. & Yoo, K.-H. Metal-insulator crossover in multilayered MoS_2. *Nanoscale* **7**, 15127–15133 (2015).
[40] Piatti, E. *et al.* Multi-valley superconductivity in ion-gated MoS_2 layers. *Nano Lett.* **18**, 4821–4830 (2018).
[41] Wu, C.-L. *et al.* Gate-induced metal-insulator transition in MoS_2 by solid superionic conductor LaF_3. *Nano Lett.* **18**, 2387–2392 (2018).
[42] Qiu, H. *et al.* Hopping transport through defect-induced localized states in molybdenum disulphide. *Nat. Commun.* **4**, 2642 (2013).
[43] Chen, J.-H., Jang, C., Xiao, S., Ishigami, M. & Fuhrer, M. S. Intrinsic and extrinsic performance limits of graphene devices on SiO_2. *Nat. Nanotechnol.* **3**, 206–209 (2008).
[44] Sarkar, S. *et al.* Role of different scattering mechanisms on the temperature dependence of transport in graphene. *Sci. Rep.* **5**, 16772 (2015).
[45] Hwang, E. H. & Das Sarma, S. Acoustic phonon scattering limited carrier mobility in two-dimensional extrinsic graphene. *Phys. Rev. B* **77**, 115449 (2008).
[46] Efetov, D. K. & Kim, P. Controlling electron-phonon interactions in graphene at ultrahigh carrier densities. *Phys. Rev. Lett.* **105**, 256805 (2010).
[47] Park, C.-H. *et al.* Electron–phonon interactions and the intrinsic electrical resistivity of graphene. *Nano Lett.* **14**, 1113–1119 (2014).
[48] Gonnelli, R. S. *et al.* Temperature dependence of electric transport in few-layer graphene under large charge doping induced by electrochemical gating. *Sci. Rep.* **5**, 9554 (2015).
[49] Gonnelli, R. S. *et al.* Weak localization in electric-double-layer gated few-layer graphene. *2D Mater.* **4**, 035006 (2017).
[50] Jiang, X. *et al.* Two-dimensional MXenes: from morphological to optical, electric, and magnetic properties and applications. *Phys. Rep.* **848**, 1–58 (2020).
[51] Khazaei, M., Ranjbar, A., Arai, M., Sasaki, T. & Yunoki, S. Electronic properties and applications of MXenes: a theoretical review. *J. Mater. Chem. C* **5**, 2488–2503 (2017).
[52] Wang, Y., Xu, Y., Hu, M., Ling, H. & Zhu, X. MXenes: focus on optical and electronic properties and corresponding applications. *Nanophotonics* **9**, 1601–1620 (2020).

[53] Halim, J. *et al.* Transparent conductive two-dimensional titanium carbide epitaxial thin films. *Chem. Mater.* **26**, 2374–2381 (2014).

[54] Miranda, A., Halim, J., Barsoum, M. W. & Lorke, A. Electronic properties of freestanding $Ti_3C_2T_x$ MXene monolayers. *Appl. Phys. Lett.* **108**, 033102 (2016).

[55] Lipatov, A. *et al.* Effect of synthesis on quality, electronic properties and environmental stability of individual monolayer Ti_3C_2 MXene flakes. *Adv. Electron. Mater.* **2**, 1600255 (2016).

[56] Dillon, A. D. *et al.* Highly conductive optical quality solution-processed films of 2D titanium carbide. *Adv. Funct. Mater.* **26**, 4162–4168 (2016).

[57] Li, G. *et al.* Equilibrium and non-equilibrium free carrier dynamics in 2D $Ti_3C_2T_x$ MXenes: THz spectroscopy study. *2D Mater.* **5**, 035043 (2018).

[58] Sangwan, V. K. & Hersam, M. C. Electronic transport in two-dimensional materials. *Annu. Rev. Phys. Chem.* **69**, 299–325 (2018).

[59] Bonaccorso, F., Bartolotta, A., Coleman, J. N. & Backes, C. 2D-crystal-based functional inks. *Adv. Mater.* **28**, 6136–6166 (2016).

[60] Mott, N. F. & Davis, E. A. *Electronic Processes in Non-crystalline Materials* (Oxford University Press, Oxford, 1979).

[61] Mott, N. F. *Metal-Insulator Transition* (Taylor & Francis, London, 1990).

[62] Heeger, A. J. The critical regime of the metal-insulator transition in conducting polymers: Experimental studies. *Phys. Scr.* **2002**, 30 (2002).

[63] Piatti, E., Romanin, D., Daghero, D. & Gonnelli, R. S. Two-dimensional hole transport in ion-gated diamond surfaces: A brief review. *Low Temp. Phys.* **45**, 1345–1359 (2019).

[64] Ashcroft, N. W. & Mermin, N. D. *Solid State Physics* (Saunders College, Philadelphia, 1976).

[65] Ando, T., Fowler, A. B. & Stern, F. Electronic properties of two-dimensional systems. *Rev. Mod. Phys.* **54**, 437 (1982).

[66] Beenakker, C. W. J. & van Houten, H. Quantum transport in semiconductor nanostructures. *Solid State Phys.* **44**, 1–228 (1991).

[67] Bergmann, G. Physical interpretation of weak localization: A time-of-flight experiment with conduction electrons. *Phys. Rev. B* **28**, 2914 (1983).

[68] Larkin, A. I. & Khmelnitsky, D. E. Anderson localization and anomalous magnetoresistance at low temperatures. *Sov. Phys.–Usp.* **25**, 185 (1982).

[69] Altshuler, B. L., Aronov, A. G. & Lee, P. A. Interaction effects in disordered Fermi systems in two dimensions. *Phys. Rev. Lett.* **44**, 19 (1980).

[70] Fukuyama, H. *Electron–electron Interactions in Disordered Systems* (North Holland, Amsterdam, 1985).

[71] Kondo, J. Resistance minimum in dilute magnetic alloys. *Prog. Theor. Phys.* **32**, 37–49 (1964).

[72] Katayama, Y. & Tanaka, S. Resistance anomaly and negative magnetoresistance in *n*-type InSb at very low temperatures. *Phys. Rev.* **153**, 873–882 (1967).

[73] Beloborodov, I. S., Lopatin, A. V. & Vinokur, V. M. Coulomb effects and hopping transport in granular metals. *Phys. Rev. B* **72**, 125121 (2005).

[74] Beloborodov, I. S., Efetov, K. B., Lopatin, A. V. & Vinokur, V. M. Transport properties of granular metals at low temperatures. *Phys. Rev. Lett.* **91**, 246801 (2003).

[75] Beloborodov, I. S., Lopatin, A. V. & Vinokur, V. M. Universal description of granular metals at low temperatures granular fermi liquid. *Phys. Rev. B* **70**, 205120 (2004).

[76] Chui, T., Deutscher, G., Lindenfeld, P. & McLean, W. L. Conduction in granular aluminum near the metal-insulator transition. *Phys. Rev. B* **23**, 6172(R) (1981).

[77] Adkins, C. J. Conduction in granular metals–variable-range-hopping in a Coulomb gap? *J. Phys. Condens. Matter.* **1**, 1253 (1989).

[78] Entin-Wohlman, O., Gefen, Y. & Shapira, Y. Variable-range hopping conductivity in granular materials. *J. Phys. C: Solid State Phys.* **16**, 1161 (1983).

[79] Affronte, M. *et al.* Low temperature electronic transport in RuO_2-based cermet resistors. *J. Low Temp. Phys.* **109**, 461–475 (1997).

[80] Grimaldi, C., Ryser, P. & Strässler, S. Gauge factor of thick-film resistors: Outcomes of the variable-range-hopping model. *J. Appl. Phys.* **88**, 4164–4169 (2000).

[81] van Staveren, M. P. J., Brom, H. B. & De Jongh, L. J. Metal-cluster compounds and universal features of the hopping conductivity of solids. *Phys. Rep.* **208**, 1–96 (1991).

[82] Halim, J. *et al.* Variable range hopping and thermally activated transport in molybdenum-based MXenes. *Phys. Rev. B* **98**, 104202 (2018).

[83] Hart, J. L. *et al.* Control of MXenes' electronic properties through termination and intercalation. *Nat. Commun.* **10**, 522 (2019).

[84] Kovtun, A. *et al.* Multiscale charge transport in van der Waals thin films: Reduced graphene oxide as a case study. *ACS Nano* **15**, 2654–2667 (2021).

[85] Ippolito, S. *et al.* Covalently interconnected transition metal dichalcogenide networks via defect engineering for high-performance electronic devices. *Nat. Nanotechnol.* **16**, 592–598 (2021).

[86] Wang, F. *et al.* Inter-flake quantum transport of electrons and holes in inkjet-printed graphene devices. *Adv. Funct. Mater.* **31**, 2007478 (2021).

[87] Bostwick, A. *et al.* Quasiparticle transformation during a metal-insulator transition in graphene. *Phys. Rev. Lett.* **103**, 056404 (2009).

[88] Chen, J.-H., Cullen, W. G., Jang, C., Fuhrer, M. S. & Williams, E. D. Defect scattering in graphene. *Phys. Rev. Lett.* **102**, 236805 (2009).

[89] Ponomarenko, L. A. *et al.* Tunable metal-insulator transition in double-layer graphene heterostructures. *Nat. Phys.* **7**, 958–961 (2011).

[90] Piatti, E., Galanti, F., Pippione, G., Pasquarelli, A. & Gonnelli, R. S. Towards the insulator-to-metal transition at the surface of ion-gated nanocrystalline diamond films. *Eur. Phys. J. Spec. Top.* **228**, 689–696 (2019).

[91] Kim, J. S. *et al.* Electrical transport properties of polymorphic MoS_2. *ACS Nano* **10**, 7500–7506 (2016).

[92] Yildiz, A., Serin, N., Serin, T. & Kasap, M. Crossover from nearest-neighbor hopping conduction to Efros-Shklovskii variable-range hopping conduction in hydrogenated amorphous silicon films. *Jpn. J. Appl. Phys.* **48**, 111203 (2009).

[93] Joung, D. & Khondaker, S. I. Efros-Shklovskii variable-range hopping in reduced graphene oxide sheets of varying carbon sp^2 fraction. *Phys. Rev. B* **86**, 235423 (2012).

[94] Elias, D. C. *et al.* Control of graphene's properties by reversible hydrogenation: evidence for graphane. *Sci-*

ence **323**, 610–613 (2009).

[95] Liu, C.-I. *et al.* Variable range hopping and nonlinear transport in monolayer epitaxial graphene grown on SiC. *Semicond. Sci. Technol.* **31**, 105008 (2016).

[96] Chen, Z. *et al.* Tunable spin-orbit interaction in trilayer graphene exemplified in electric-double-layer transistors. *Nano Lett.* **12**, 2212–2216 (2012).

[97] Chen, J.-H., Li, L., Cullen, W. G., Williams, E. D. & Fuhrer, M. S. Tunable Kondo effect in graphene with defects. *Nat. Phys.* **7**, 535–538 (2011).

[98] Tikhonenko, F. V., Horsell, D. W., Gorbachev, R. V. & Savchenko, A. K. Weak localization in graphene flakes. *Phys. Rev. Lett.* **100**, 056802 (2008).

[99] Kozikov, A. A., Savchenko, A. K., Narozhny, B. N. & Shytov, A. V. Electron-electron interactions in the conductivity of graphene. *Phys. Rev. B* **82**, 075424 (2010).

[100] Neal, A. T., Liu, H., Gu, J. & Ye, P. D. Magneto-transport in MoS_2: Phase coherence, spin-orbit scattering, and the Hall factor. *ACS Nano* **7**, 7077–7082 (2013).

[101] Schmidt, H. *et al.* Quantum transport and observation of Dyakonov-Perel spin-orbit scattering in monolayer MoS_2. *Phys. Rev. Lett.* **116**, 046803 (2016).

[102] Du, Y., Neal, A. T., Zhou, H. & Peide, D. Y. Transport studies in 2D transition metal dichalcogenides and black phosphorus. *J. Phys. Condens. Matter.* **28**, 263002 (2017).

[103] Ouisse, T. & Barsoum, M. W. Magnetotransport in the MAX phases and their 2D derivatives: MXenes. *Mater. Res. Lett.* **5**, 365–378 (2017).

[104] Barua, S., Hatnean, M. C., Lees, M. & Balakrishnan, G. Signatures of the Kondo effect in VSe_2. *Sci. Rep.* **7**, 10964 (2017).

[105] Yu, Z. *et al.* Analyzing the carrier mobility in transition-metal dichalcogenide MoS_2 field-effect transistors. *Adv. Funct. Mater.* **27**, 1604039 (2017).

[106] Piatti, E., Chen, Q., Tortello, M., Ye, J. & Gonnelli, R. S. Possible charge-density-wave signatures in the anomalous resistivity of li-intercalated multilayer MoS_2. *Appl. Surf. Sci.* **461**, 269–275 (2018).

[107] Romanin, D., Brumme, T., Daghero, D., Gonnelli, R. S. & Piatti, E. Strong band-filling-dependence of the scattering lifetime in gated MoS_2 nanolayers induced by the opening of intervalley scattering channels. *J. Appl. Phys.* **128**, 063907 (2020).

[108] Kravets, V. G. *et al.* Spectroscopic ellipsometry of graphene and an exciton-shifted van Hove peak in absorption. *Phys. Rev. B* **81**, 155413 (2010).

[109] Eda, G. *et al.* Photoluminescence from chemically exfoliated MoS_2. *Nano Lett.* **11**, 5111–5116 (2011).

[110] Wilcoxon, J. P., Newcomer, P. P. & Samara, G. A. Synthesis and optical properties of MoS_2 and isomorphous nanoclusters in the quantum confinement regime. *J. Appl. Phys.* **81**, 7934–7944 (1997).

[111] Hu, M. *et al.* Surface functional groups and interlayer water determine the electrochemical capacitance of $Ti_3C_2T_x$ MXene. *ACS Nano* **12**, 3578–3586 (2018).

[112] Hope, M. A. *et al.* NMR reveals the surface functionalisation of Ti_3C_2 MXene. *Phys. Chem. Chem. Phys.* **18**, 5099–5102 (2016).

[113] Satheeshkumar, E. *et al.* One-step solution processing of Ag, Au and Pd@ MXene hybrids for SERS. *Sci. Rep.* **6**, 32049 (2016).

[114] El-Demellawi, J. K., Lopatin, S., Yin, J., Mohammed, O. F. & Alshareef, H. N. Tunable multipolar surface plasmons in 2D $Ti_3C_2T_x$ MXene flakes. *ACS Nano* **12**, 8485–8493 (2018).

[115] Hantanasirisakul, K. & Gogotsi, Y. Electronic and optical properties of 2D transition metal carbides and nitrides (MXenes). *Adv. Mater.* **30**, 1804779 (2018).

[116] Liu, G. *et al.* Surface modified Ti_3C_2 MXene nanosheets for tumor targeting photothermal/photodynamic/chemo synergistic therapy. *ACS Appl. Mater. Interfaces* **9**, 40077–40086 (2017).

[117] Hoath, S. D. *Fundamentals of Inkjet Printing: The Science of Inkjet and Droplets* (John Wiley & Sons, 2016).

[118] Sarycheva, A. & Gogotsi, Y. Raman spectroscopy analysis of the structure and surface chemistry of $Ti_3C_2T_x$ MXene. *Chem. Mater.* **32**, 3480–3488 (2020).

[119] Kang, R. *et al.* Enhanced thermal conductivity of epoxy composites filled with 2D transition metal carbides (MXenes) with ultralow loading. *Sci. Rep.* **9**, 9135 (2019).

[120] Myhra, S., Crossley, J. A. A. & Barsoum, M. W. Crystal-chemistry of the Ti_3AlC_2 and Ti_4AlN_3 layered carbide/nitride phases—characterization by XPS. *J. Phys. Chem. Solids* **62**, 811–817 (2001).

[121] Halim, J. *et al.* X-ray photoelectron spectroscopy of select multi-layered transition metal carbides (MXenes). *Appl. Surf. Sci.* **362**, 406–417 (2016).

[122] Schier, V., Michel, H.-J. & Halbritter, J. ARXPS-analysis of sputtered TiC, SiC and $Ti_{0.5}Si_{0.5}C$ layers. *Fresenius J. Anal. Chem.* **346**, 227–232 (1993).

[123] García-Romeral, N., Keyhanian, M., Morales-García, Á. & Illas, F. Relating X-ray photoelectron spectroscopy data to chemical bonding in MXenes. *Nanoscale Adv.* **3**, 2793–2801 (2021).

[124] Natu, V. *et al.* A critical analysis of the x-ray photoelectron spectra of $Ti_3C_2T_z$ MXenes. *Matter* **4**, 1224–1251 (2021).

[125] Ferrari, A. C. *et al.* Raman spectrum of graphene and graphene layers. *Phys. Rev. Lett.* **97**, 187401 (2006).

[126] Casiraghi, C. *et al.* Raman spectroscopy of graphene edges. *Nano Lett.* **9**, 1433–1441 (2009).

[127] Ferrari, A. C. & Basko, D. M. Raman spectroscopy as a versatile tool for studying the properties of graphene. *Nat. Nanotechnol.* **8**, 235–246 (2013).

[128] Kholmanov, I. N. *et al.* Improved electrical conductivity of graphene films integrated with metal nanowires. *Nano Lett.* **12**, 5679–5683 (2012).

[129] Secor, E. B., Ahn, B. Y., Gao, T. Z., Lewis, J. A. & Hersam, M. C. Rapid and versatile photonic annealing of graphene inks for flexible printed electronics. *Adv. Mater.* **27**, 6683–6688 (2015).

[130] Parkin, W. M. *et al.* Raman shifts in electron-irradiated monolayer MoS_2. *ACS Nano* **10**, 4134—-4142 (2016).

[131] Acerce, M., Voiry, D. & Chhowalla, M. Metallic 1T phase MoS_2 nanosheets as supercapacitor electrode materials. *Nat. Nanotechnol.* **10**, 313–318 (2015).

[132] De, S., King, P. J., Lyons, P. E., Khan, U. & Coleman, J. N. Size effects and the problem with percolation in nanostructured transparent conductors. *ACS Nano* **4**, 7064–7072 (2010).

[133] De, S. & Coleman, J. N. The effects of percolation in nanostructured transparent conductors. *MRS Bulletin* **36**, 774–781 (2011).

[134] Carey, T. *et al.* Inkjet printed circuits with 2D semiconductor inks for high-performance electronics. *Adv. Electron. Mater.* 2100112 (2021).

[135] Wang, H., Wu, Y., Cong, C., Shang, J. & Yu, T. Hysteresis of electronic transport in graphene transistors. *ACS Nano* **4**, 7221–7228 (2010).

[136] Lemme, M. C. Current status of graphene transistors. *Solid State Phenom.* **156–158**, 499–509 (2010).

[137] Emelianova, E. V., Van der Auweraer, M., Adriaenssens, G. J. & Stesmans, A. Carrier mobility in two-dimensional disordered hopping systems. *Org. Electron.* **9**, 29–135 (2008).

[138] Okada, J., Nagase, T., Kobayashi, T. & Naito, H. Temperature dependence of field-effect mobility in organic thin-film transistors: Similarity to inorganic transistors. *J. Nanosci. Nanotechnol.* **16**, 3219–3222 (2016).

[139] Sagar, R. U. R. *et al.* Large unsaturated room temperature negative magnetoresistance in graphene foam composite for wearable and flexible magnetoelectronics. *Nano Research* **12**, 101–107 (2019).

[140] Rodríguez, M., Bonalde, I. & Medina, E. Consistent hopping criterion in the Efros-Shklovskii regime. *Phys. Rev. B* **75**, 235505 (2007).

[141] Castner, T. G. & Shafarman, W. N. Deconvolution of activated and variable-range-hopping conduction for barely insulating arsenic-doped silicon. *Phys. Rev. B* **60**, 14182 (1999).

[142] Adkins, C. J., Benjamin, J. D., Thomas, J. M. D., Gardner, J. W. & McGeown, A. J. Potential disorder in granular metal systems: the field effect in discontinuous metal films. *J. Phys. C: Solid State Phys.* **17**, 4633 (1984).

[143] Su, T.-I., Wang, C.-R., Lin, S.-T. & Rosenbaum, R. Magnetoresistance of $Al_{70}Pd_{22.5}Re_{7.5}$ quasicrystals in the variable-range hopping regime. *Phys. Rev. B* **66**, 054438 (2002).

[144] Gu, H. *et al.* Separating positive and negative magnetoresistance for polyaniline-silicon nanocomposites in variable range hopping regime. *Appl. Phys. Lett.* **102**, 212403 (2013).

[145] Rosenbaum, R. *et al.* Magnetoresistance of an insulating amorphous nickel–silicon film in large magnetic fields. *Physica B* **294—295**, 340–342 (2001).

[146] Shklovskii, B. I. & Efros, A. L. *Electronic Properties of Doped Semiconductors* (Springer Verlag, Berlin, 1984).

[147] Bergmann, G. Quantitative analysis of weak localization in thin Mg films by magnetoresistance measurements. *Phys. Rev. B* **25**, 2937(R) (1982).

[148] Pippard, A. B. *Magnetoresistance in Metals* (Cambridge University Press, Cambridge, 1989).

[149] Hikami, S., Larkin, A. I. & Nagaoka, Y. Spin-orbit interaction and magnetoresistance in the two dimensional random system. *Prog. Theor. Phys.* **63**, 707–710 (1980).

[150] Bergmann, G. Weak localization in thin films: a time-of-flight experiment with conduction electrons. *Phys. Rep.* **107**, 1–58 (1984).

[151] Edmonds, M. T. *et al.* Spin–orbit interaction in a two-dimensional hole gas at the surface of hydrogenated diamond. *Nano Lett.* **15**, 16–20 (2015).

[152] Altshuler, B. L., Aronov, A. G. & Khmelnitsky, D. E. Effects of electron-electron collisions with small energy transfers on quantum localisation. *J. Phys. C: Solid State Phys.* **15**, 7367 (1982).

[153] Blanter, Y. M., Vinokur, V. M. & Glazman, L. I. Weak localization in metallic granular media. *Phys. Rev. B* **73**, 165322 (2006).

[154] Biagini, C., Caneva, T., Tognetti, V. & Varlamov, A. A. Weak localization effects in granular metals. *Phys. Rev. B* **72**, 041102(R) (2005).

[155] Vilkman, M., Lankinen, A., Volk, N., Kostamo, P. & Ikkala, O. Self-assembly of cationic rod-like poly (2, 5-pyridine) by acidic bis (trifluoromethane) sulfonimide in the hydrated state: A highly-ordered self-assembled protonic conductor. *Polymer* **51**, 4095–4102 (2010).

[156] Piatti, E. *et al.* Ambipolar suppression of superconductivity by ionic gating in optimally doped $BaFe_2(As,P)_2$ ultrathin films. *Phys. Rev. Materials* **3**, 044801 (2019).

[157] Ooi, N., Rairkar, A. & Adams, J. B. Density functional study of graphite bulk and surface properties. *Carbon* **44**, 231–242 (2006).